



**HAL**  
open science

## Zonal shear and super-rotation in a magnetized spherical Couette flow experiment

Daniel Brito, Thierry Alboussière, Philippe Cardin, Nadège Gagnière, Dominique Jault, Patrick La Rizza, Jean-Paul Masson, Henri-Claude Nataf, Denys Schmitt

► **To cite this version:**

Daniel Brito, Thierry Alboussière, Philippe Cardin, Nadège Gagnière, Dominique Jault, et al.. Zonal shear and super-rotation in a magnetized spherical Couette flow experiment. 2011. hal-00569377v1

**HAL Id: hal-00569377**

**<https://hal.science/hal-00569377v1>**

Preprint submitted on 24 Feb 2011 (v1), last revised 16 May 2011 (v2)

**HAL** is a multi-disciplinary open access archive for the deposit and dissemination of scientific research documents, whether they are published or not. The documents may come from teaching and research institutions in France or abroad, or from public or private research centers.

L'archive ouverte pluridisciplinaire **HAL**, est destinée au dépôt et à la diffusion de documents scientifiques de niveau recherche, publiés ou non, émanant des établissements d'enseignement et de recherche français ou étrangers, des laboratoires publics ou privés.

1 **Zonal shear and super-rotation in a magnetized spherical Couette**  
2 **flow experiment**

3 D. Brito

4 *Laboratoire des Fluides Complexes et leurs Réservoirs,*  
5 *Université de Pau et des Pays de l'Adour,*  
6 *CNRS, BP 1155, 64013 Pau Cedex France\**

7 T. Alboussière,<sup>†</sup> P. Cardin, N. Gagnière, D. Jault, P.

8 La Rizza, J.-P. Masson, H.-C. Nataf, and D. Schmitt

9 *Institut des Sciences de la Terre, CNRS,*  
10 *Observatoire de Grenoble, Université Joseph-Fourier,*  
11 *Maison des Géosciences, BP 53, 38041 Grenoble Cedex 9, France*

12 (Dated: February 24, 2011)

## Abstract

13

14 We present measurements performed in a spherical shell filled with liquid sodium, where a 74 mm-  
15 radius inner sphere is rotated while a 210 mm-radius outer sphere is at rest. The inner sphere holds  
16 a dipolar magnetic field and acts as a magnetic propeller when rotated. In this experimental set-up  
17 called *DTS*, direct measurements of the velocity are performed by ultrasonic Doppler velocimetry.  
18 Differences in electric potential and the induced magnetic field are also measured to characterize  
19 the magnetohydrodynamic flow. Rotation frequencies of the inner sphere are varied between -  
20 30 Hz and +30 Hz, the magnetic Reynolds number based on measured sodium velocities and on  
21 the shell radius reaching to about 33. We have investigated the mean axisymmetric part of the  
22 flow, which consists in differential rotation. Strong super-rotation of the fluid with respect to the  
23 rotating inner sphere is directly measured. It is found that the organization of the mean flow  
24 does not change much throughout the entire range of parameters covered by our experiment. The  
25 direct measurements of zonal velocity give a nice illustration of Ferraro's law of isorotation in the  
26 vicinity of the inner sphere where magnetic forces dominate inertial ones. The transition from a  
27 Ferraro regime in the interior to a geostrophic regime, where inertial forces predominate, in the  
28 outer regions has been well documented. It takes place where the local Elsasser number is about  
29 1. A quantitative agreement with non-linear numerical simulations is obtained when keeping the  
30 same Elsasser number. The experiments also reveal a region that violates Ferraro's law just above  
31 the inner sphere.

---

\*formerly member of the geodynamo team (Institut des Sciences de la Terre); daniel.brito@univ-pau.fr

†now at : Laboratoire de Sciences de la Terre, ENS Lyon, CNRS, Lyon, France

## 32 I. INTRODUCTION

33 The Earth's fluid core below the solid mantle consists of a 3480 km-radius spherical cavity  
34 filled with a liquid iron alloy. A 1220 km-radius solid inner core sits in its center. It has  
35 been accepted since the 1940's [1, 2] that the flows stirring the electrically conducting liquid  
36 iron in the outer core produce the Earth's magnetic field by dynamo action. The fluid  
37 motion is thought to originate from the cooling of the Earth's core, which results both in  
38 crystallization of the inner core and in convection in the liquid outer core [3].

39 The last decade has seen enormous progress in the numerical computation of the geo-  
40 dynamo problem after the first simulation of a dynamo powered by convection [4–7]. It  
41 is however still unclear why many characteristics of the Earth's magnetic field are so-well  
42 retrieved with simulations [8] since the latter are performed with values of important di-  
43 mensionless parameters that differ much from the appropriate values for the Earth's core.  
44 The main numerical difficulty is the simultaneous computation of the velocity, the magnetic  
45 and the temperature fields with realistic diffusivities, respectively the fluid viscosity, the  
46 magnetic and the thermal diffusivities. Those differ indeed by six orders of magnitude in  
47 the outer core [9]; such a wide range is at present out of reach numerically, the simulations  
48 being performed at best with two orders of magnitude difference between the values of the  
49 diffusivities. An experimental approach of the geodynamo is, in that respect, promising since  
50 the fluid metals used in experiments have physical properties, specifically diffusivities, very  
51 close to the properties of the liquid iron alloy in the Earth's outer core. Moreover, experi-  
52 ments and simulations are complementary since they span different ranges of dimensionless  
53 parameters.

54 Magnetohydrodynamics experiments devoted to the dynamo study have started some 50  
55 years ago (see the chapter authored by Cardin and Brito in [10] for a review). To possibly  
56 induce magnetic fields, the working fluid must be liquid sodium in such experiments. Sodium  
57 is indeed the fluid that best conducts electricity in laboratory conditions. A breakthrough  
58 in these dynamo experiments occurred at the end of 1999 when amplification and saturation  
59 of an imposed magnetic field were measured for the first time in two experiments, in Riga  
60 [11] and in Karlsruhe [12]. The common property of those set-ups was to have the sodium  
61 motion very much constrained spatially, in order to closely follow fluid flows well known  
62 analytically to lead to a kinematic dynamo, respectively the Ponomarenko flow [13] and the

63 G.O. Robert flow [14]. More recently, the first experimental dynamo in a fully turbulent  
64 flow was obtained in a configuration where two crenelated ferromagnetic rotating discs drive  
65 a von Kàrmàn swirling flow in a cylinder [15]. Earth's like magnetic field reversals were  
66 also obtained in this experimental dynamo [16]. Other similar experiments have been run  
67 where sodium flows are driven by propellers in a spherical geometry [17, 18]. In order to  
68 emphasize the specificity of the experimental study presented in the present paper, it is  
69 worth mentioning two common features of the previously mentioned sodium experiments:  
70 the forcing of the sodium motion is always purely mechanical and the magnetic field is *weak*  
71 in the sense that Lorentz forces are small compared to the non-linear velocity terms in the  
72 equation of motion [19].

73 The experiment called *DTS* for "Derviche Tourneur Sodium" has been designed to in-  
74 vestigate a supposedly relevant regime for the Earth's core, the magnetostrophic regime  
75 [20–22] where the ratio of Coriolis to Lorentz forces is of the order one. The container made  
76 of weakly conducting stainless steel is spherical and can rotate about a vertical axis. An  
77 inner sphere consisting of a copper envelope enclosing permanent magnets is placed at the  
78 center of the outer sphere; the force free magnetic field produced by those magnets enables  
79 to explore dynamical regimes where Coriolis and Lorentz forces are comparable. The sodium  
80 motion in the spherical gap is driven by the differential rotation between the inner sphere  
81 and the outer sphere, unlike in the Earth's core where the iron motion is predominantly  
82 driven by convection [23] and maybe minorly by differential rotation of the inner core [24].

83 The *DTS* experiment has not been designed to run in a dynamo regime. It has instead  
84 been conceived as a small prototype of a possible future large sodium spherical dynamo  
85 experiment which would benefit from its results. Note than meanwhile Daniel Lathrop and  
86 collaborators have built a 3m-diameter sodium spherical experiment with an inner sphere  
87 differentially rotating with respect to the outer sphere, like in *DTS*. Schaeffer, Cardin and  
88 Guervilly [25, 26] have shown numerically that a dynamo could occur in a spherical Couette  
89 flow at large  $Rm$  in a low magnetic Prandtl number fluid such as sodium ( $Pm = \nu/\lambda$  (see  
90 TABLE I)).

91 Numerical simulations in a *DTS*-type configuration [27–29] of Couette spherical flows  
92 with an imposed magnetic field all show azimuthal flows stabilized by magnetic and rotation  
93 forces. Using electric potential measurements along a meridian of the outer sphere boundary,  
94 we concluded in our first report of *DTS* experimental results [30] that the amplitude of the

95 azimuthal flow may exceed the velocity of sodium in solid body rotation with the inner  
96 sphere, as predicted theoretically in the linear regime [31].

97 The *DTS* experiment offers a tool to investigate non uniform rotation of an electrically  
98 conducting fluid in the presence of rotation and magnetic forces. The differential rotation  
99 of a body permeated by a strong magnetic field and the waves driven by the non uniform  
100 rotation have received considerable attention since the work of Ferraro [32, 33]. Indeed,  
101 the absence of solid envelopes makes non uniform rotation possible in stars, where it plays  
102 an important role in the mixing of chemical elements [34], in contrast with the case of  
103 planetary fluid cores. Ferraro found that the angular rotation in an electrically conducting  
104 body permeated by a steady magnetic field symmetric about the axis of rotation tends to  
105 be constant along magnetic lines of force. MacGregor and Charbonneau [35] illustrated  
106 this result and showed, in a weakly rotating case, that Ferraro's theorem holds for  $\text{Ha} \gg 1$   
107 ( $\text{Ha}$ , the Hartmann number, measures the magnetic strength (see TABLE II). An intense  
108 magnetic field, probably of primordial origin, is the key actor in the transfer of angular  
109 momentum from the solar radiative interior to the convection zone [36, 37]. Finally, in  
110 a geophysical context, Aubert recently found, investigating zonal flows in spherical shell  
111 dynamos, that Ferraro's law of isorotation gives a good description of the geometry of the  
112 zonal flows of thermal origin [38].

113 In the second study of the *DTS* experiment [39], we investigated azimuthal flows when  
114 both the inner boundary and the outer boundary are rotating but at different speeds, using  
115 Doppler velocimetry and electric potential measurements. Specifically, we discussed the  
116 transition between the outer geostrophic region and the inner region where magnetic forces  
117 dominate. Extending the asymptotic model of Kleorin *et al* [40], we could explain the  
118 shape of the measured azimuthal velocity profiles. We had to use a specific electric potential  
119 difference as a proxy of the differential rotation between the two spheres as, unfortunately,  
120 the electrical coupling between the liquid sodium and the copper casing of the interior  
121 magnets was apparently both imperfect and unreliable. Finally, we reported in on our third  
122 article [41] about the *DTS* experiment the presence of azimuthally traveling hydromagnetic  
123 waves that we inferred mainly from electric potential measurements along parallels.

124 We investigate here again the main flows when the outer sphere is at rest. Our new study  
125 benefits from a comparison with our earlier work [39] for a rotating outer sphere. There is no  
126 need any more to use an indirect measure of the global rotation of the fluid as the electrical

127 coupling between liquid sodium and copper has become unimpaired. Furthermore, the *DTS*  
128 experiment has been equipped with a host of new measurement tools. The flow amplitude  
129 is measured along 7 different beams using Doppler velocimetry. Assuming axisymmetry, we  
130 have thus been able to map the azimuthal flow in most of the fluid. It turns out that the  
131 electric potential differences evolve monotonically with the inner core rotation but cannot  
132 be interpreted directly as a measure of the velocity below the outer viscous boundary layer.  
133 We have also entered a probe inside the cavity to measure the induced magnetic field in  
134 the interior. The dense measurements in the *DTS* experiment give a nice illustration of  
135 the Ferraro law of isorotation [32] in the inner region where magnetic forces dominate. In the  
136 outer region, we retrieve axially invariant azimuthal flow as the Proudman-Taylor theorem  
137 holds there. The variation of the geostrophic velocity with the distance to the axis differs  
138 nevertheless from the case of a rotating outer sphere as recirculation in the outer Ekman  
139 layer plays an important role in the latter case.

140 The organisation of the paper is as follows. In section II, we describe the experimental set-  
141 up and the techniques that we use to measure the magnetic, electric and velocity fields; we  
142 illustrate them with a discussion of a typical experimental run. In section III, we present the  
143 governing equations and the relevant dimensionless numbers of the experiment. We devote  
144 one section of the article to the observation of differential rotation and another one to the  
145 meridional circulation. Then, the experimental measurements are compared to numerical  
146 simulations of *DTS*. We summarize and discuss the results of our study in section VII.

## 147 II. THE *DTS* EXPERIMENT

### 148 A. The experimental set-up

149 The *DTS* experimental set-up [30, 39, 41] is shown in FIG. 1. It has been installed in a  
150 small building purpose-designed for sodium experiments.

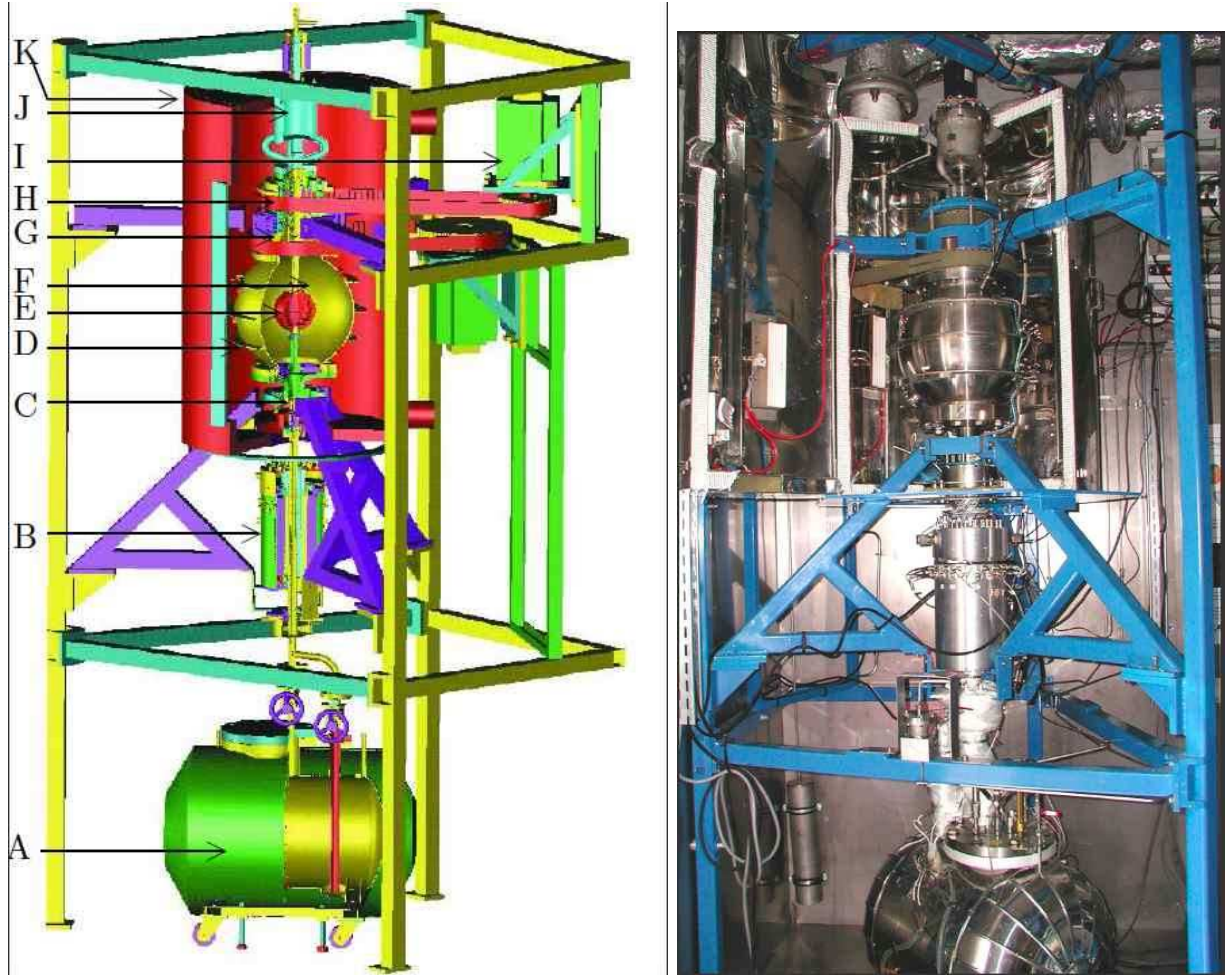


FIG. 1. Diagram and picture of the experimental set-up. A: moveable sodium reservoir, B: shielded electric slip-ring, C: electromagnetic valve, D: outer sphere, E: magnetized rotating inner sphere, F: spherical shell containing liquid sodium, G: magnetic coupling entraining the inner sphere shaft, H: crenelated belt, I: brushless electric motor driving the inner sphere, J: expansion tank for sodium, K: thermostated chamber. The total height of the set-up is 3.9 m.

151 As shown in FIG. 1, liquid sodium is contained in a spherical shell between an outer  
152 sphere and an inner sphere. The radius of the outer sphere is  $a = 210$  mm and that of the



153 inner sphere  $b = 74$  mm. The outer sphere is made of stainless steel and is 5 mm thick.  
 154 The copper inner sphere (FIG. 2 and FIG. 3) contains magnetized Rare-Earth cobalt bricks  
 155 assembled such that the resulting permanent magnetic field is very close to an axial dipole  
 156 of moment intensity  $|\mathcal{M}| = 700 \text{ Am}^2$ , with its axis of symmetry aligned with the axis of  
 157 rotation. The magnetic field points downward along the rotation axis and its magnitude  
 158 ranges from 345 mT at the poles of the inner sphere down to 8 mT at the equator of the  
 159 outer sphere.

160 Sodium is kept most of the time in the reservoir at the bottom of the set-up. When  
 161 needed to run an experiment, liquid sodium is melted and pushed up from that reservoir  
 162 into the spherical shell by imposing an overpressure of Argon in the reservoir. When liquid  
 163 sodium reaches the expansion tank at the top of the spherical shell, an electromagnetic  
 164 valve located just below the sphere (see FIG. 1) is locked such that sodium is kept in the  
 165 upper part during experiments. In case of emergency, the valve is opened and sodium pours  
 166 directly into the reservoir.

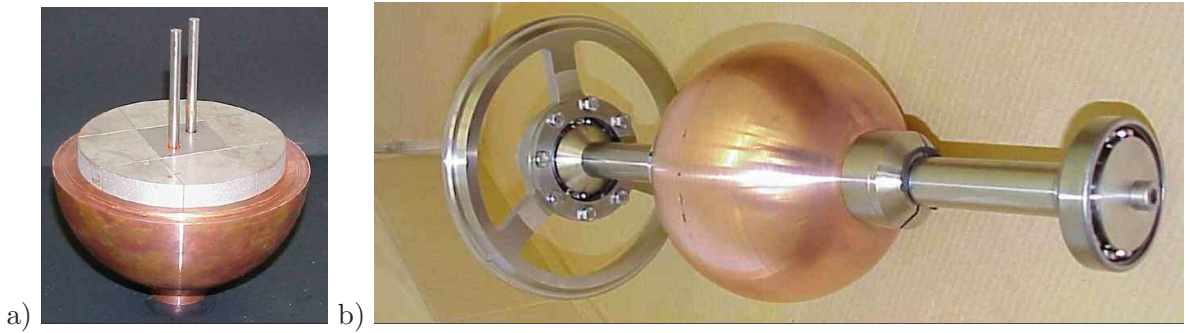


FIG. 2. a) Picture of one hemisphere of the inner sphere. Different pieces of magnets in gray are assembled in the bulk of the inner sphere. b) View from the side of the inner sphere and its rotating shaft. Note that the wheels at the top and bottom (only one is shown in the picture) of the rotating shaft are attached to the outer sphere.

167 The central part of the experiment is air-conditioned in a chamber maintained at around  
 168  $130^\circ\text{C}$  during experiments: four 1 kW infrared radiants disposed around the outer sphere  
 169 heat the chamber, whereas cold air pumped from outside cools the set-up when necessary.  
 170 Liquid sodium is therefore usually kept some  $30^\circ\text{C}$  above its melting temperature during  
 171 experiments. Some physical properties of sodium relevant to our study are listed in TABLE I.  
 172 The whole volume containing sodium, from the reservoir tank up to the expansion tank is

TABLE I. Physical properties of pure liquid sodium at 130°C (Documents from CEA, Commissariat l'énergie atomique et aux énergies alternatives). \*The sound velocity in sodium has been precisely measured in the present study using the UDV apparatus.

$\rho$	density	$9.3 \cdot 10^2 \text{ kg m}^{-3}$
$\sigma$	electric conductivity	$9 \cdot 10^6 \text{ } \Omega^{-1} \text{ m}^{-1}$
$\nu$	kinematic viscosity	$6.5 \cdot 10^{-7} \text{ m}^2\text{s}^{-1}$
$\eta$	magnetic diffusivity	$8.7 \cdot 10^{-2} \text{ m}^2\text{s}^{-1}$
$c$	sound velocity*	$2.45 \cdot 10^3 \text{ m s}^{-1}$

173 kept under Argon pressure at all times in order to limit oxidization of sodium.

174 The rotation of the inner sphere, between  $f = -30 \text{ Hz}$  and  $f = 30 \text{ Hz}$ , is driven by  
175 a crenelated belt attached to a 11 kW brushless motor (SGMH-1ADCA61 from Yaskawa  
176 Electric Corporation, Tokyo, Japan). The belt entrains a home-made magnetic coupler  
177 located around the inner sphere shaft as seen in FIG. 1. The coupler is composed of an  
178 array of magnets located outside the sodium container, another array of magnets inside the  
179 container being immersed in liquid sodium. The inner magnets are anchored to the rotating  
180 shaft of the inner sphere such that when the belt is rotated outside, the inner sphere is  
181 rotated as well. Such a coupler has the advantage of not requiring any rotating seal in liquid  
182 sodium. Torque values up to about 70 Nm have been efficiently transmitted through this  
183 coupler in the experiment.

## 184 B. Measurements

### 185 1. Ultrasonic Doppler velocimetry

186 We use UDV ultrasonic Doppler velocimetry [42] in order to measure liquid sodium ve-  
187 locities in the spherical shell. This non intrusive technique has been intensively used in our  
188 group for the last decade, in particular in rotating experiments performed either in water or  
189 in liquid metals [43–46]. The technique consists in the emission from a piezoelectric trans-  
190 ducer of a succession of bursts of ultrasonic waves that propagate in the fluid. When the  
191 wave encounters a particle with a different acoustic impedance, part of the ultrasonic wave  
192 is backscattered towards the transducer. The time elapsed between the emitted and the  
193 reflected wave and the change in that time respectively give the position of the particle with  
194 respect to the transducer and the fluid velocity along the beam direction. Data process-  
195 ing is internal to the DOP2000 apparatus (<http://www.signal-processing.com>, Signal  
196 Processing company, Lausanne, Switzerland).

197 The ultrasonic probes are held in circular stainless steel caps attached to the outer sphere,  
198 as shown in FIG. 3a). There are six locations with interchangeable caps on the outer sphere  
199 such that fluid velocities can be measured from any of these different positions. The thickness  
200 of the stainless steel wall between the probes and liquid sodium has been very precisely  
201 machined to 1.4 mm in order to insure the best transmission of energy from the probe to the  
202 fluid [47]. Small sodium oxides and/or gas bubbles are present and backscatter ultrasonic  
203 waves as in gallium experiments [46]. We keep the surface of the caps in contact with sodium  
204 as clean as possible to perform UDV measurements.

205 We use high temperature 4 MHz ultrasonic transducers (TR0405AH from Signal Pro-  
206 cessing) 10 mm long and 8 or 12 mm in diameter (piezoelectric diameter 5 or 7 mm). The  
207 measurements shown throughout the paper were performed with pulse repetition frequency  
208 (*prf*) varying from 3 kHz to 12 kHz and with a number of *prf* per profile varying from 8 to  
209 128. A present limitation of this UDV technique is that the maximum measurable veloc-  
210 ity obeys the following function  $u_{\max} = c^2/4f_e P_{\max}$  where  $c$  is the ultrasonic velocity of the  
211 medium,  $f_e$  is the emitting frequency, and  $P_{\max}$  is the maximum measurable depth along  
212 the velocity profile. Applying this relationship to the parameters used in *DTS*,  $P_{\max} \simeq 200$   
213 mm (approximative length of the first half of the beam in Figure 3) and  $f_e = 4$  Mhz, the

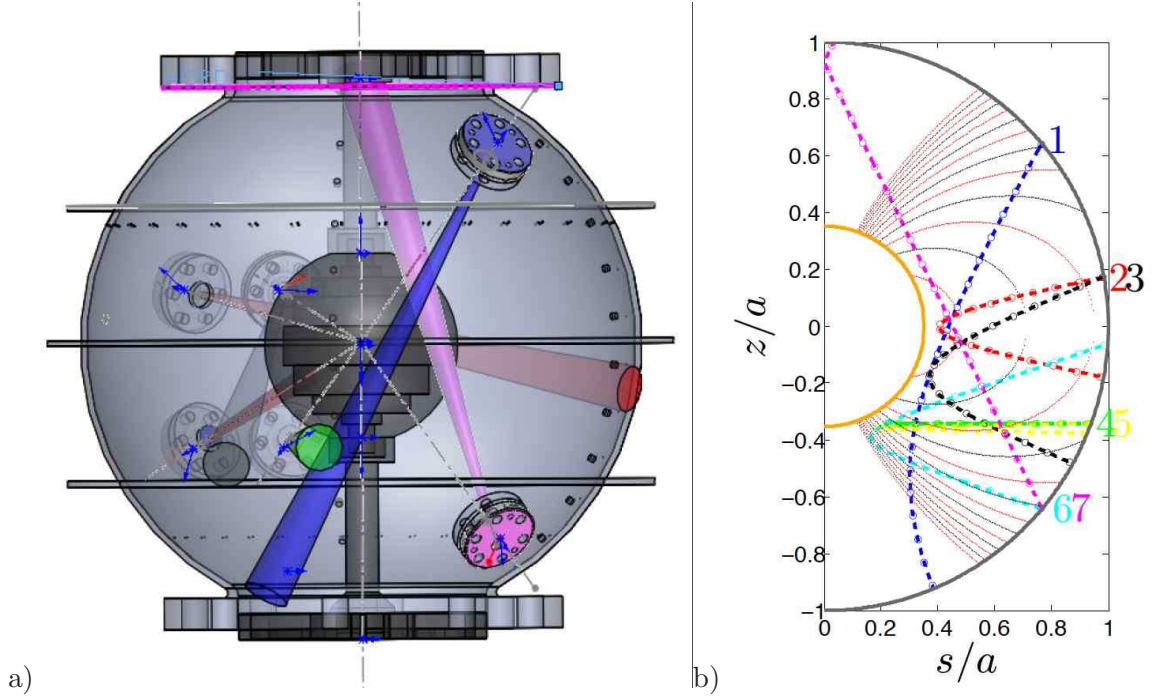


FIG. 3. a) 3D perspective view of the outer sphere and its interior. Caps at various latitudes hold ultrasonic velocity probes to perform UDV. The divergent ultrasonic beams emitted from each cap are shown in perspective with different colors. The five superimposed horizontal slices of magnets are assembled in the heart of the inner sphere. Differences in electric potential are measured between points from latitude  $+45^\circ$  to latitude  $-45^\circ$ , with steps of  $10^\circ$  (holes along a meridian at the right of the Figure). b) Meridional view of the normalized coordinates  $(s/a, z/a)$  covered by the ultrasonic trajectories numbered from 1 to 7. Some of the corresponding rays are plotted in Figure a) with the same color code. The distance  $d$  from the outer sphere along the ultrasonic beam is marked by small dots drawn every 20 mm. The dipolar magnetic field lines are drawn from  $L=1.4$  to  $9.6$  ( $L$  is defined in section IV A). The first line attached to the inner sphere equator in red is  $L=1.4$  and then  $L$  increases as the lines emerge closer to the poles.

214 maximum measurable velocity is of the order 2.2 m/s. In particular cases, it is possible to  
 215 overcome this limitation by using aliased profiles of velocity [43] as shown later in the paper.  
 216 The spatial resolution of the velocity profiles is about 1 mm, and the velocity resolution is  
 217 about 0.5%, or better for the aliased profiles.

218 We have measured both the radial and oblique components of velocity in the bulk of the  
 219 spherical shell. The radial measurements were performed from the latitudes  $+10^\circ$ ,  $-20^\circ$  and

220  $-40^\circ$ . The oblique measurements were performed from different locations and in different  
 221 planes, along rays that all deviate from the radial direction by the same angle ( $24^\circ$ ). Thus,  
 222 they all have the same length in the fluid cavity. At the point of closest approach, the rays  
 223 are 11 mm away from the inner sphere. The seven oblique beams used in *DTS* are sketched  
 224 in FIG. 3b). The way to retrieve the meridional and azimuthal components of the velocity  
 225 field along the ultrasonic beam is detailed in the Appendix.

226 We use UDV measurements to confirm the strong magnetic coupling between the inner  
 227 rotating sphere and sodium. In a smaller version of *DTS* performed in water, maximum  
 228 angular velocities (normalized by that of the inner sphere) of the order 0.16 are obtained  
 229 for a hydrodynamic Reynolds number of  $10^5$  in the vicinity of the equatorial plane, close  
 230 to the rotating inner sphere [26]. For similar Re in *DTS*, sodium is in super-rotation close  
 231 to the inner rotating sphere and maximum measured velocities are instead around 1.2 (see  
 232 FIG. 11b) for example).

## 233 2. *Magnetic field inside the sphere*

234 The measurement technique described so far does not requires probes that protrude inside  
 235 the sphere. In order to measure the magnetic field inside the sphere, in the liquid, we have  
 236 installed magnetometers inside a sleeve, which enters deep into the liquid. The external  
 237 dimensions of the sleeve are 114 mm (length inside the sphere) and 16 mm (diameter). It  
 238 contains a board equipped with high-temperature Hall magnetometers (model A1384LUA-T  
 239 of Allegro Microsystems Inc). We measure the radial component of the magnetic field at  
 240 radii (normalized by  $a$  the inner radius of the outer sphere) 0.93 and 0.74. The orthoradial  
 241 component is measured at 0.97 and 0.78, and the azimuthal component at 0.99, 0.89, 0.79,  
 242 0.69, 0.60 and 0.50. The sleeve is mounted in place of a removable port (at a latitude of  
 243 either  $40^\circ$ ,  $10^\circ$  or  $-20^\circ$ ). A top view of the sleeve is shown in FIG. 6. The measured voltage  
 244 is sampled at 2000 samples/second with a 16-bit 250 kHz PXI-6229 National Instruments  
 245 acquisition card. The precision of the measurements (estimated from actual measurements  
 246 when  $f = 0$ ) is about  $140\mu\text{T}$ , and corresponds to about 20 bits of the A/D converter.  
 247 Magnetic fields up to 60mT have been measured.

248 3. *Differences in electric potentials on the outer sphere*

249 Differences in electric potentials are measured along several meridians and along one  
 250 parallel of the outer sphere [30, 39, 41]). In the present study, we are interested in the  
 251 measurements performed along meridians since they are linked to the azimuthal flow velocity  
 252  $u_\varphi$  (we denote  $(r, \theta, \varphi)$  the spherical coordinates). The measurements are performed between  
 253 successive electrodes located from  $-45^\circ$  to  $+45^\circ$  in latitude, with electrodes  $10^\circ$  apart as  
 254 sketched in FIG. 3a). We note  $\Delta V_{40} = V_{45} - V_{35}$  the difference between the electric potential  
 255 at latitudes  $45^\circ$  and  $35^\circ$ . Electric potentials are measured by electrodes soldered to brass  
 256 bolts 3 mm long, those being screwed into 1 mm-diameter, 4 mm-deep blind holes drilled in  
 257 the stainless steel wall of the outer sphere. The measured voltage is filtered by an RC anti-  
 258 aliasing 215 Hz low-pass filter and then sampled at 1000 samples/second with a 16-bit 250  
 259 kHz PXI-6229 National Instruments acquisition card. The precision of the measurements  
 260 (estimated from actual measurements at  $f = 0$ ) is about  $80\mu\text{V}$ , and corresponds to about  
 261 10 bits of the A/D converter. Electric potential differences up to 7mV have been measured.

262 Denoting  $\mathbf{E}$  the electric field, we introduce the electric potential  $V$  through  $\mathbf{E} = -\nabla V$ ,  
 263 which is valid in a steady state. Then, the electric potential measurements are analysed using  
 264 Ohm's law for a moving conductor,  $\mathbf{j} = \sigma(\mathbf{u} \times \mathbf{B} + \mathbf{E})$  where  $\sigma$  is the electric conductivity,  
 265  $\mathbf{j}$  the electric current density vector,  $\mathbf{u}$  the velocity field and  $\mathbf{B}$  the magnetic field. If the  
 266 meridional electric currents  $j_\theta$  are small compared to  $\sigma u_\varphi B_r$  in the fluid interior and away  
 267 from the equatorial plane where  $B_r = 0$ , and if the viscous boundary layer adjacent to the  
 268 outer sphere is thin, which ensures the continuity of  $E_\theta$  through the layer, then the measured  
 269 differences in electric potential depend on the product of the local radial magnetic field  $B_r$   
 270 by  $u_\varphi$ , the azimuthal fluid velocity:

$$\frac{\Delta V}{a\Delta\theta} = u_\varphi B_r, \quad (1)$$

271 where  $\Delta\theta = 10^\circ$  is the angle between two electrodes. However, we shall question below the  
 272 assumption on the smallness of  $j_\theta$ , referred to as the frozen flux hypothesis.

273 4. *Velocity and torque measured from the motor driving the inner sphere*

274 The electronic drive of the motor entraining the inner sphere delivers an analog signal  
 275 for its angular velocity and its torque. We checked and improved the velocity measurement

276 by calibrating it using a rotation counter, which consists of a small magnet glued on the  
277 entrainment pellet and passing once per turn in front of a magnetometer. The torque signal  
278 is used to infer the power consumption in section IID.

### 279 C. A typical experiment : a complete set of measurements

280 A complete set of measurements performed during a typical experiment is analyzed below.  
281 The run was chosen to illustrate the various measurements but also to depict how the  
282 different observables evolve with  $f$ . During that run of 600 seconds, the inner sphere was  
283 first accelerated from 0 to  $f = 30$  Hz in around 120 seconds, then decelerated back to 0 during  
284 120 seconds. The inner sphere was then kept at rest for about 100 seconds and accelerated  
285 in the opposite direction to  $f = -30$  Hz in 120 seconds. It returned to zero rotation in 120  
286 seconds again. That cycle of rotation is shown in FIG. 4. The torque delivered by the inner  
287 sphere motor is also shown and evolves clearly non-linearly during those cycles.

288 FIG. 4 shows electric potential records (see part IIB3) obtained during that experiment  
289 and time averaged over 0.1 s windows. The differences of potential vary in sync with the inner  
290 sphere rotation frequency as expected if the various  $\Delta V$  measure the differential rotation  
291 between the liquid sodium and the outer sphere to which the electrodes are affixed (IIB3).  
292 However, it is also apparent that the fluid rotation as measured from the  $\Delta V$ s does not  
293 increase linearly with the inner sphere frequency. We interpret it as an indication that  
294 braking at the outer boundary, which opposes the entrainment by the inner core rotation,  
295 varies non linearly with the differential rotation. As expected, records from electrodes pairs  
296 are anti-symmetrical with respect to the equator, since the forcing is symmetrical while the  
297 radial component of the imposed magnetic field changes sign across the equator.

298 FIG. 5 shows the fluid velocity  $u(d)$  measured by UDV during the first half of the exper-  
299 iment along the ray 6 as a function of time and distance. Velocity profiles were recorded  
300 along a total distance  $d \simeq 90$  mm. As demonstrated in FIG. 5b), the velocity is aliased  
301 since the maximum measurable velocity, for the ultrasonic frequency used during the exper-  
302 iment, is exceeded. Since the azimuthal velocity profiles are quite simple in shape, it has  
303 been straightforward to unfold those profiles and retrieve the correct amplitudes as shown in  
304 FIG. 5c). The evolution with  $f$  is similar to that of the electrodes, but indicates a stronger  
305 leveling-off as  $f$  increases.

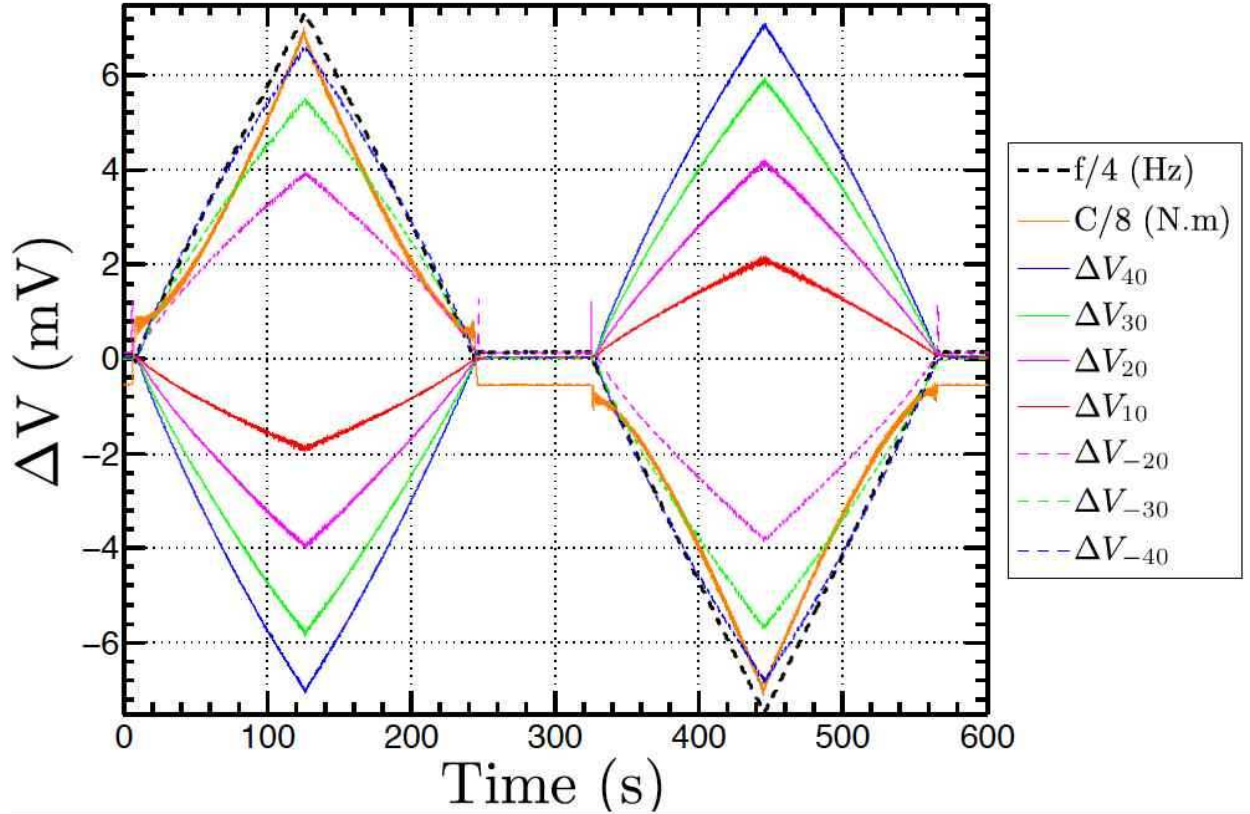


FIG. 4. Records of the inner core rotation frequency  $f$ , torque  $C$  and differences in electric potential  $\Delta V_{40}$ ,  $\Delta V_{30}$ ,  $\Delta V_{20}$ ,  $\Delta V_{10}$ ,  $\Delta V_{-20}$ ,  $\Delta V_{-30}$ ,  $\Delta V_{-40}$  as a function of time. The subscript denotes the latitude (in degrees) of the electric potential difference.

306 FIG. 6 shows the magnetic field induced inside the fluid during the typical experiment.  
 307 The measurements are taken in the sleeve placed at  $40^\circ$  latitude. The induced azimuthal field  
 308 (FIG. 6 a)) is measured at 6 different radii (given in section II B 2). Its intensity reaches  
 309 60 mT near the inner sphere and gets larger than the imposed dipole in some locations.  
 310 Note the simple evolution with  $f$ , which contrasts with that of the electric potentials and  
 311 velocities in that it increases with an exponent larger than 1. The induced meridional field  
 312 (FIG. 6) is more than 10 times weaker. It is dominated by fluctuations, and does not change  
 313 sign when  $f$  does. Note that the evolution with  $f$  is not monotonic. Similar behaviors are  
 314 observed at latitudes  $10^\circ$  and  $-20^\circ$ .



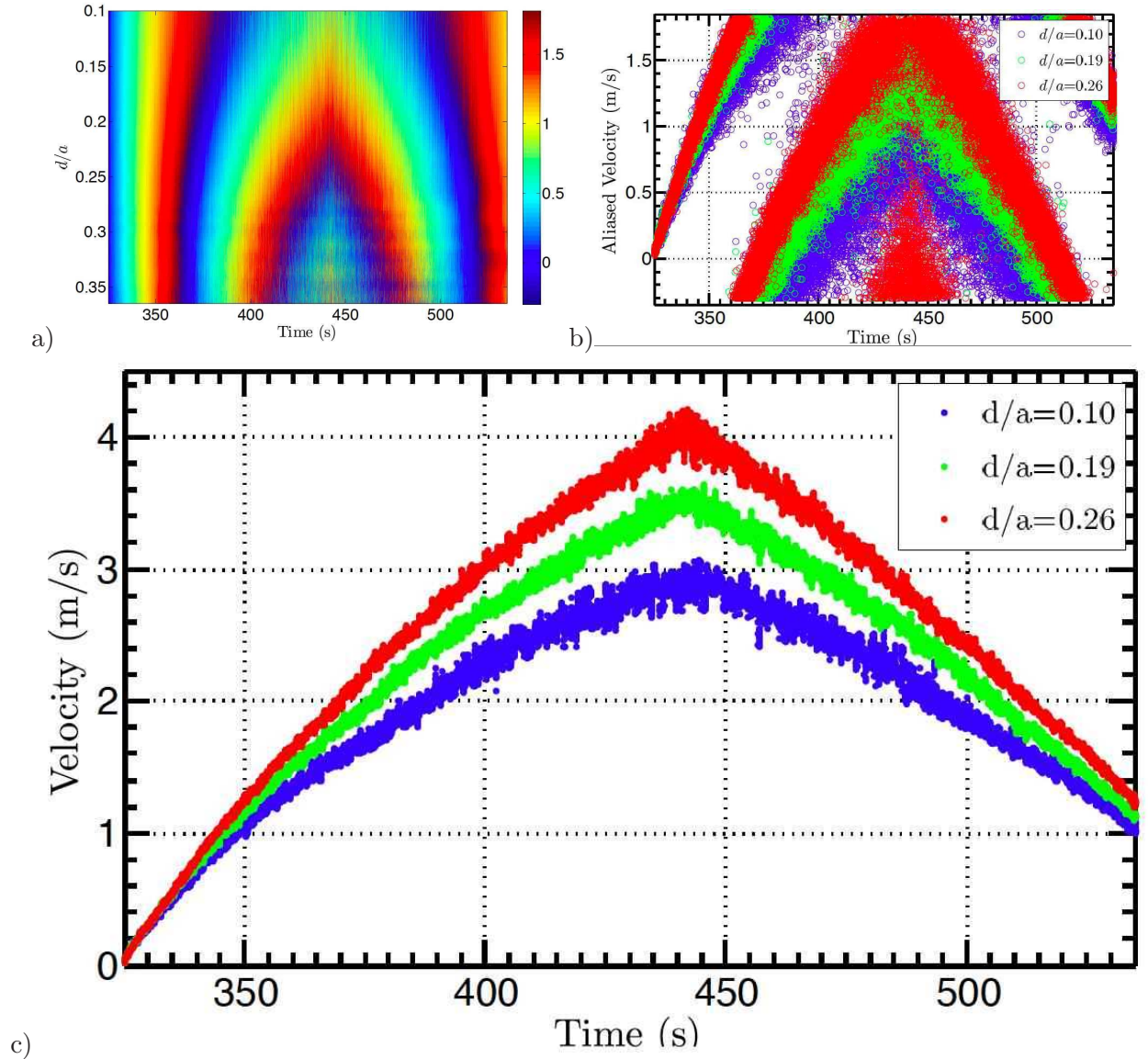


FIG. 5. UDV measurements performed along the ray number 6 (see FIG. 3) during the second half of the typical experiment when the inner sphere was rotated from rest to -30 Hz and then back to rest. a) Spatio-temporal representation of the measured velocity, given by the color scale (in m/s). b) Velocity at three distances from the probe as a function of time, extracted from the spatio-temporal Figure a). The velocity profiles are clearly aliased since the profiles are discontinuous. c) After applying a median time-filtering window of 0.2 s and unfolding the profiles, the correct velocities are retrieved as a continuous function of time.

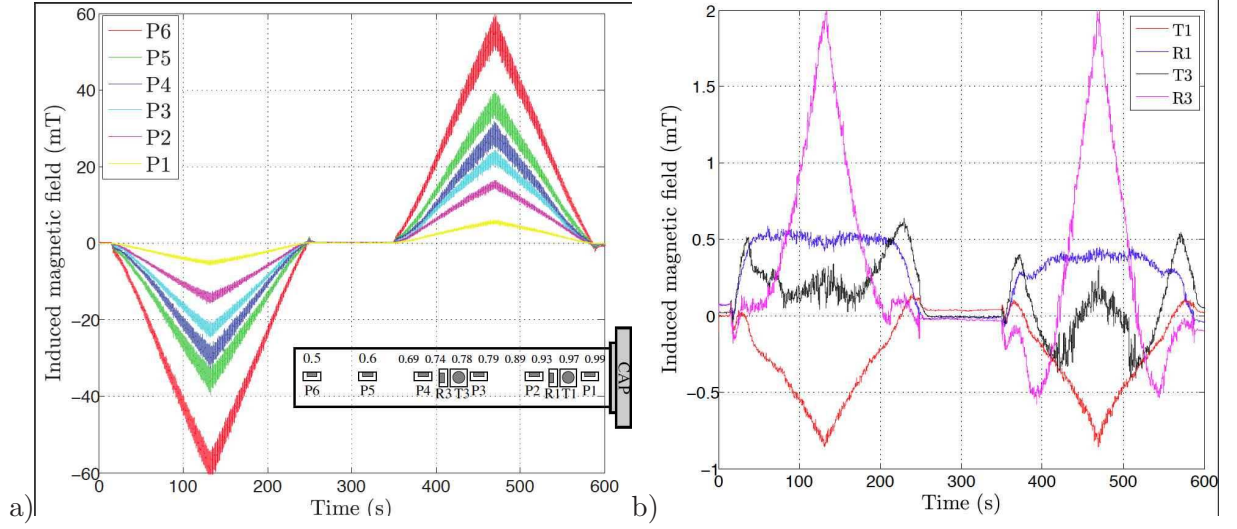


FIG. 6. a) Azimuthal  $b_\varphi$ , b) radial  $b_r$  and orthoradial  $b_\theta$  induced magnetic field at a latitude of  $40^\circ$  in the sleeve at different radial positions recorded during the two triangles sequence of FIG. 4. A top view of the sleeve at the bottom of Figure a) gives the radial position and the orientation of the various Hall magnetometers. The intensity of the induced azimuthal field reaches 60 mT near the inner sphere and has the sign of  $-f$  (because the imposed dipolar field has its south pole in the northern hemisphere). The fluctuations reach about 10% of the mean. The meridional components of the induced magnetic field are much weaker and dominated by fluctuations, which have been filtered out here (0.2 Hz low-pass filter).

#### 315 **D. Power scaling**

316 The power dissipated by the flow is shown in FIG. 7 as a function of the rotation frequency  
317  $f$ . It is computed from the product  $\Gamma \times 2\pi f$ , where  $\Gamma$  is the torque retrieved from the motor  
318 drive. We subtracted the power measured with an empty shell (dash-dot curve) to eliminate  
319 power dissipation in the mechanical set-up. The dissipation in the fluid reaches almost 8 kW  
320 for the highest rotation frequency of the inner sphere ( $f = \pm 30$  Hz). The small spread of  
321 the data dots indicates that power fluctuations are small. The continuous line is the record  
322 of power versus  $f$  when the inner sphere is ramped from 0 to  $-30$  Hz as in FIG. 4. The  
323 corresponding increase in kinetic energy only slightly augments power dissipation.

324 Power dissipation is found to scale as  $f^{2.4}$ , and indicates weak turbulence. An exponent  
325 3 is expected for fully turbulent flows with mechanical forcing [48].

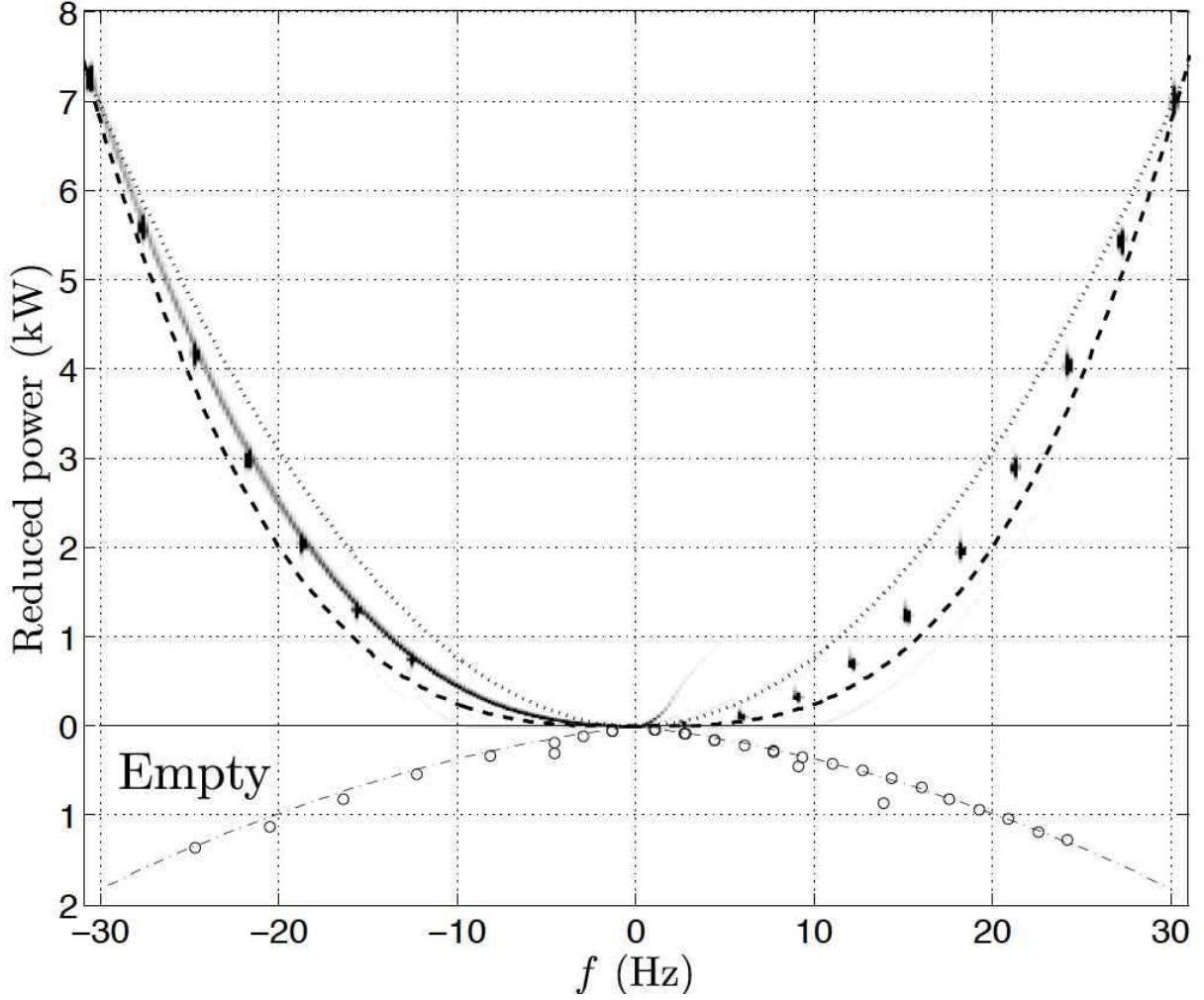


FIG. 7. Power dissipated by the flow in *DTS*. The data dots are from measurements of the motor torque for plateaus at given  $f$ . The dissipation in the mechanical set-up has been removed. It is obtained by rotating the inner sphere before filling the shell with sodium. It is drawn here upside-down in the lower panel (empty symbols) and can be fit by  $\mathcal{P}_{\text{empty}}(\text{W}) = 4 \times |2\pi f| + 0.03 \times (2\pi f)^2$  (dash-dot curve). Dissipation in the flow scales as  $f^{2.4}$ , and is here compared with  $f^2$  (dotted line) and  $f^3$  (dashed line).

### 326 III. GOVERNING EQUATIONS

A spherical shell of inner radius  $b$  and outer radius  $a$  is immersed in an axisymmetric dipolar magnetic field  $\mathbf{B}_d$ :

$$\mathbf{B}_d(r, \theta, \varphi) = -B_0 \left(\frac{b}{r}\right)^3 [2 \cos \theta \mathbf{e}_r + \sin \theta \mathbf{e}_\theta],$$

327 where  $(r, \theta, \varphi)$  are spherical coordinates. The outer boundary is kept at rest and the inner  
 328 sphere rotates with the constant angular velocity  $\Omega = 2\pi f$  along the same axis as the dipole  
 329 field that it carries. We assume that the electrically conducting fluid filling the cavity is  
 330 homogeneous, incompressible and isothermal. We further assume that the flow inside the  
 331 cavity is steady.

332 The inner body consists of a magnetized innermost core enclosed in an electrically con-  
 333 ducting spherical solid envelope of finite thickness  $d_b$ . We choose  $b$  as unit length,  $b\Omega$  as unit  
 334 velocity,  $\rho b^2 \Omega^2$  as unit pressure, and  $b^2 \Omega B_0 / \eta = \text{Rm} B_0$  as unit of induced magnetic field  $\mathbf{b}$   
 335 ( $\mathbf{B} = \mathbf{B}_d + \text{Rm} \mathbf{b}$ ). Then, the equations governing the flow  $\mathbf{u}$  and the induced magnetic field  
 336 are:

$$\nabla \cdot \mathbf{u} = 0 \tag{2}$$

$$\nabla \cdot \mathbf{b} = 0 \tag{3}$$

$$(\mathbf{u} \cdot \nabla) \mathbf{u} = -\nabla p + \Lambda ((\mathbf{B}_d \cdot \nabla) \mathbf{b} + (\mathbf{b} \cdot \nabla) \mathbf{B}_d) + \text{Re}^{-1} \nabla^2 \mathbf{u} \tag{4}$$

$$\nabla^2 \mathbf{b} = -\nabla \times (\mathbf{u} \times \mathbf{B}), \tag{5}$$

337 where  $p$  is a modified pressure. The notation  $\Lambda$  refers to the Elsasser number, classically  
 338 used for rotating flows in the presence of a magnetic field. That number  $\Lambda$  compares the  
 339 magnetic and inertial forces in the vicinity of the magnetized inner sphere. In the shell  
 340 interior, the two forces are better compared by a "local" Elsasser number:  $\Lambda_l = (b/r)^6 \Lambda$   
 341 (with  $(b/a)^6 \simeq 1.83 \cdot 10^{-3}$ ). Finally, it is of interest to introduce the Hartmann number  
 342  $\text{Ha}$  that compares the magnetic and viscous forces. We have  $\text{Ha} = (\Lambda \text{Re})^{1/2}$ . In the shell  
 343 interior, the number  $(b/r)^3 \text{Ha}$  is more appropriate to compare the two forces. Typical values  
 344 of these dimensionless numbers can be found in TABLE II.

345 The set of equations (2-5), where the non linear terms are neglected, was the subject of the  
 346 analytical study of Dormy et al. [31] that described how the differential rotation between the

TABLE II. Typical values of the dimensionless numbers in the *DTS* experiment, computed for  $f = \Omega/2\pi = 25$  Hz.

Re	$b^2\Omega/\nu$	$1.3 \cdot 10^6$
Rm	$b^2\Omega/\eta$	10
$\Lambda$	$\sigma B_0^2/\rho\Omega$	1.9
Ha	$(\text{Re}\Lambda)^{1/2}$	$1.6 \cdot 10^3$

fluid interior and the outer sphere drives an influx of electrical currents from the mainstream into the outer viscous Hartmann boundary layer. Electrical currents flow along the viscous boundary layer and return to the conducting inner body along a free shear layer located on the magnetic field line tangent to the outer boundary at the equator. As these electrical currents cannot flow exactly parallel to the magnetic field line, they produce a Lorentz force, which sustains "super-rotation" of the fluid. Recent studies have extended the analysis to the case of a finitely conducting outer sphere [49, 50]. On increasing the conductance of the container, more and more electrical currents leak into the solid boundary and the super-rotation rate gets as large as  $O(\text{Ha}^{1/2})$ . Though the analytical results have set the stage for the interpretation of the experimental results, the neglected non linear effects are crucial in the *DTS* experiment, even for the smallest rate of rotation of the solid inner body.

Upon reversal of  $\Omega$ ,  $u_\varphi$  and  $b_\varphi$  change into  $-u_\varphi$  and  $-b_\varphi$  whilst the other components of  $\mathbf{u}$  and  $\mathbf{b}$  are kept unchanged.

#### IV. DIFFERENTIAL ROTATION

##### A. Transition between the Ferraro and geostrophic regimes

In that section, we use the UDV records to delve into the geometry of isorotation surfaces. The L number associated to each dipolar magnetic field line enters the equation of the surfaces spanned by dipolar lines of force:

$$r = L \sin^2 \theta . \quad (6)$$

FIG. 8 shows that, for  $L \leq 2.7$ , the angular velocity measured along rays 2 and 3, which are the most appropriate to map the azimuthal velocity field, is, to a large extent, a function

367 of  $L$  only. Thus, the angular velocity does not vary along magnetic field lines near the inner  
 368 sphere, where the magnetic field is the strongest. We interpret this result as a consequence  
 369 of Ferraro's theorem of isorotation. The latter is written:

$$\mathbf{B}_a \cdot \nabla \left( \frac{u_\varphi}{s} \right) = 0. \quad (7)$$

370 It is obtained from the  $\varphi$  component of the induction equation for steady fields, ignoring  
 371 magnetic diffusion. Although often invoked in the framework of ideal MHD (where magnetic  
 372 diffusion is negligible), Ferraro's law does not require a large  $Rm$  [51]. It implies that there  
 373 is no induced magnetic field and that, as a consequence, the magnetic force is exactly zero.  
 374 More precisely, deviations from this law lead to the induction of a magnetic field, which  
 375 produces a magnetic force that tends to oppose this induction process. Writing  $\mathbf{u} = \mathbf{u}_0 + \mathbf{u}_1$ ,  
 376 where  $\mathbf{u}_0$  obeys the equation (7), we obtain  $b \approx u_1$  from (5). Then, the momentum equation  
 377 (4) yields  $u_1 \approx (\text{Re}\Lambda)^{-1}u_0 = \text{Ha}^{-1}u_0$  (as numerically verified in [35]) when the inertial term,  
 378 on the left hand side, can be neglected. Ferraro's law of isorotation, though, is not the only  
 379 way to cancel the magnetic force. In the presence of electric currents parallel to the magnetic  
 380 field, the magnetic force remains zero and the equation (7) can be violated [50, 51]. For the  
 381 geometry of the *DTS* experiment, it cannot happen along the innermost dipolar field lines  
 382 that connect one parallel of the inner body surface in one hemisphere to its mirror image in  
 383 the other hemisphere, without reaching the outer sphere. Indeed, symmetry with respect to  
 384 the equatorial plane  $E$  implies that the currents do not cross  $E$ .

385 Thus, the observation of a velocity field obeying Ferraro's law is a symptom that magnetic  
 386 forces predominate in that region. Note that the fact that the two legs of the profile along  
 387 ray 2 show similar velocities even for large  $L$  only probes the symmetry of the flow with  
 388 respect to the equatorial plane.

389 Now, FIG. 9 shows that for  $s \geq 0.6$  the azimuthal velocity is largely a function of  $s$   
 390 only. There, the Proudman-Taylor theorem holds and azimuthal flows are geostrophic as  
 391 the inertial forces predominate. In contrast with the case of a rotating outer sphere (see  
 392 figure 7 in [39]), there is no region of uniform rotation: zonal velocities are  $z$ -independent  
 393 but vary with the distance to the  $z$  axis.

394 The transition between the Ferraro and geostrophic regimes (FIG. 10) occurs at smaller  
 395 distances from the axis as the rotation frequency of the inner core increases. It takes place  
 396 where the local Elsasser number  $\Lambda_l$ , which compares the magnetic and inertial forces, is of

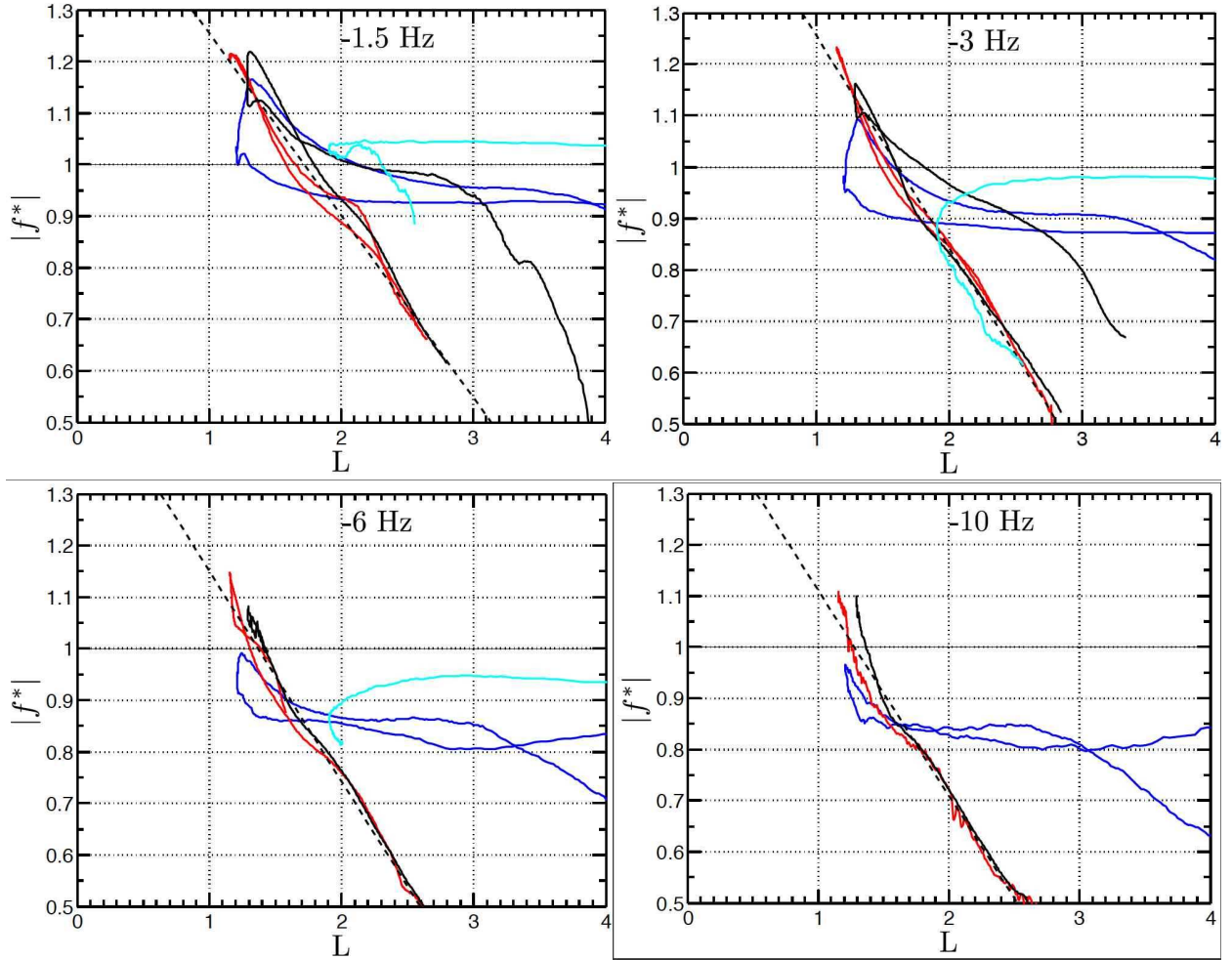


FIG. 8. Rotation frequency of the fluid sodium over the inner sphere rotation frequency as a function of the magnetic field lines  $L$  for four ultrasonic velocity profiles (trajectories 1, 2, 3 and 6, with the same color code as in FIG 3) and four inner sphere rotation frequencies ( $f = -1.5, -3, -6$  and  $-10$  Hz). The dashed line is a straight line to help the eye.

397 order 1.

398 In the geostrophic region, magnetic stress integrated on the geostrophic cylinders remains  
 399 strong enough to overcome the viscous friction at the outer boundary and to impart a rapid  
 400 rotation to the fluid but becomes weaker than the Reynolds stress (which can be represented  
 401 as a Coriolis force). As a result, the fluid angular velocity is still of the order of the angular  
 402 velocity of the inner sphere and the velocities are predominantly geostrophic.



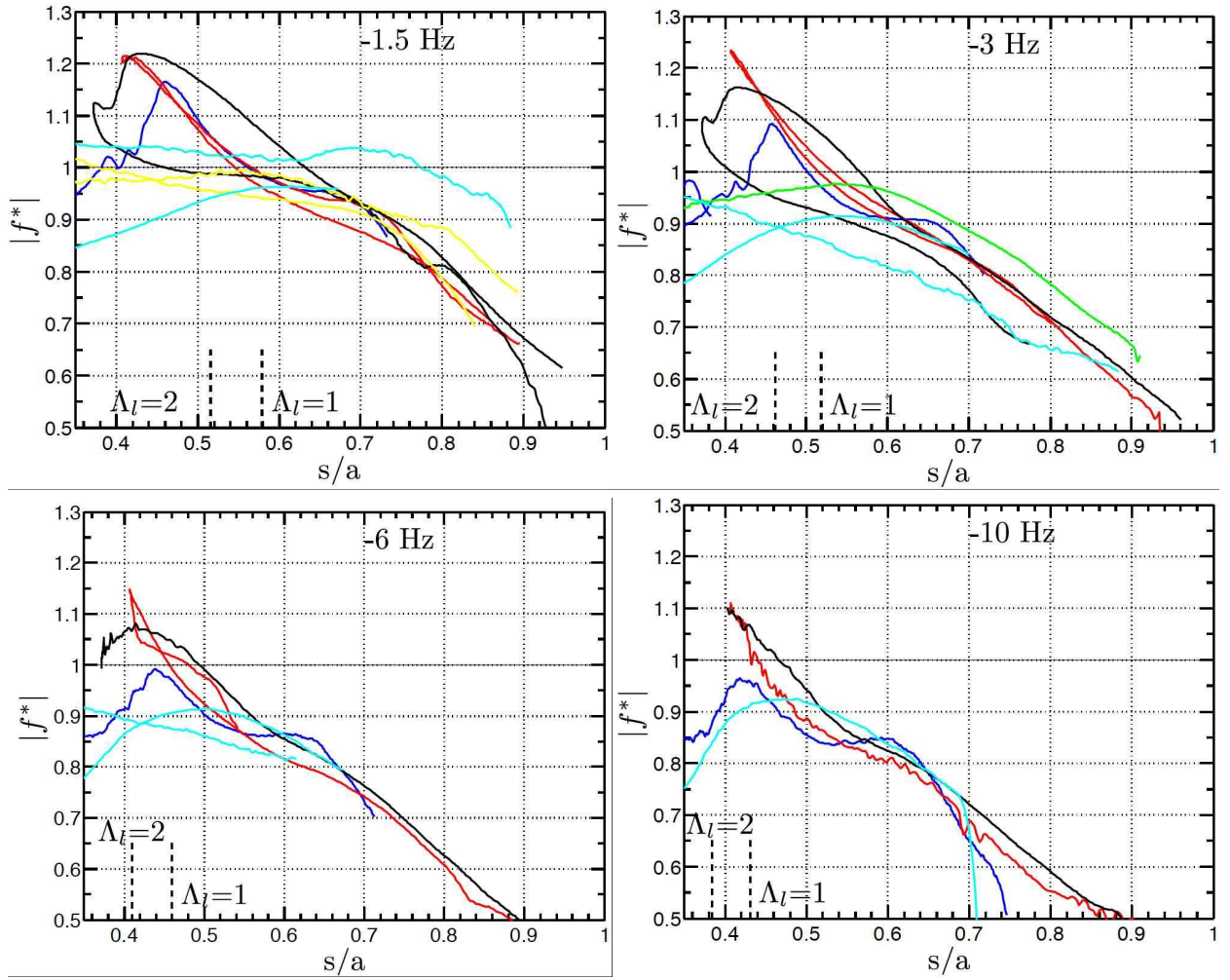


FIG. 9. Rotation frequency of the fluid sodium normalized by the inner sphere rotation frequency as a function of  $s$ , for various ultrasonic velocity profiles and four inner sphere rotation frequencies ( $f = -1.5, -3, -6$  and  $-10$  Hz). The colors of the profiles follow the conventions laid out in FIG. 3.

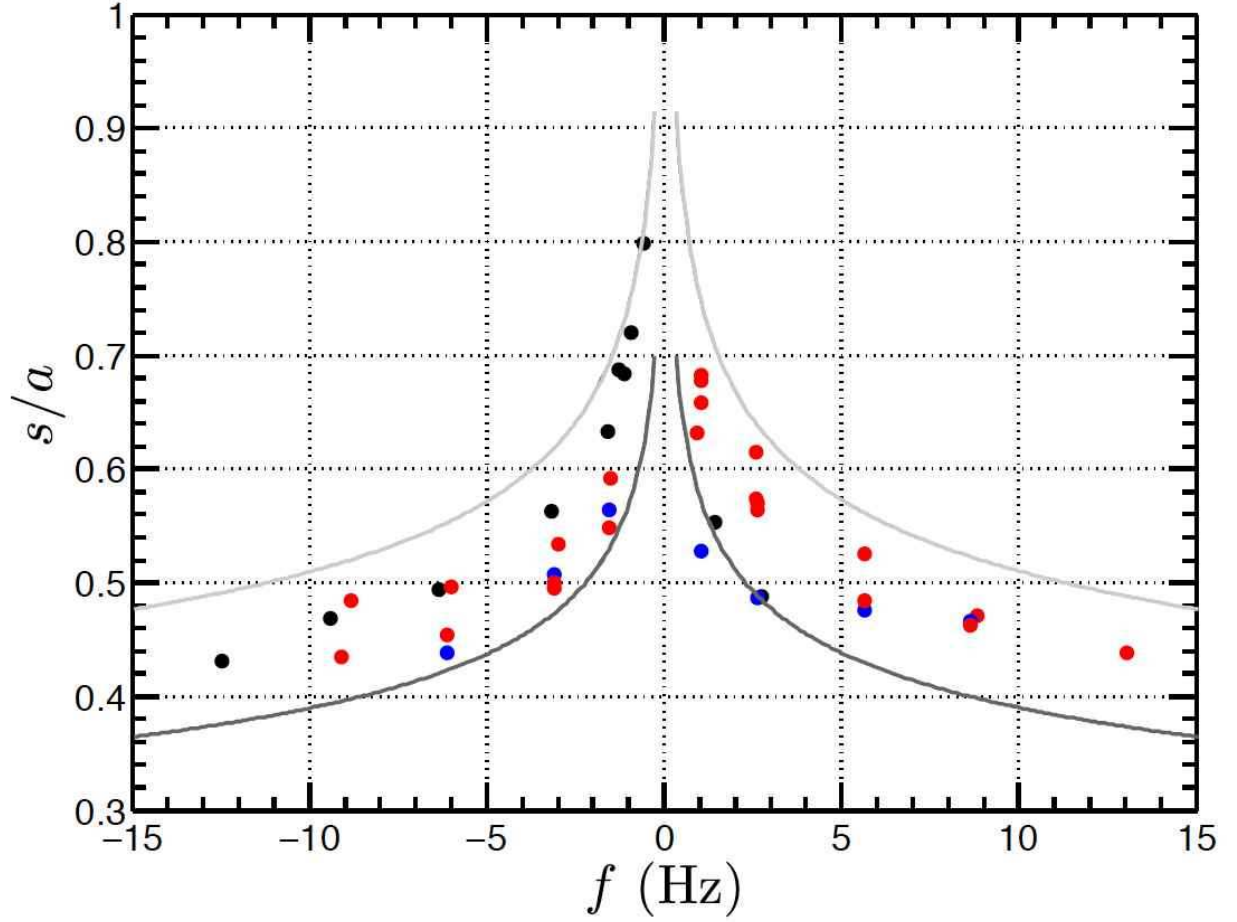


FIG. 10. Normalized cylindrical radius  $s/a$  along the UDV trajectories number 1 (blue), 2 (red) and 3 (black) where  $f_{fluid} = f$  (*i.e.*  $f^* = 1$ ) as a function of the inner sphere rotation frequency. Pale line :  $\Lambda_l = 0.5$ , Dark line :  $\Lambda_l = 2.5$ .

403 **B. Inversion of velocity profiles**

404 Flow velocity is constrained by its projection on the several ultrasonic rays that we  
 405 shoot. We invert the Doppler velocity profiles for the large scale mean flow, assuming that  
 406 the steady part of the flow is symmetric about the axis of rotation and with respect to the  
 407 equatorial plane. A poloidal/toroidal decomposition,

$$\mathbf{u} = u_\varphi \mathbf{e}_\varphi + \nabla \times (u_p \mathbf{e}_\varphi), \quad (8)$$

408 is employed. We first consider the azimuthal velocity  $u_\varphi$ , which is expanded in associated  
 409 Legendre functions with odd degree and order 1, *i.e.*

$$u_\varphi(r, \theta) = \sum_{l=0}^{l_{max}} u_\varphi^l(r) P_{2l+1}^1(\cos \theta). \quad (9)$$

410 The functions  $u_\varphi^l(r)$  are decomposed into a sum from  $k = 0$  to  $k_{max}$  of Chebyshev poly-  
 411 nomials of the second kind on the interval  $[0, 1]$  mapped onto the interval  $[b/a, 1]$ , *i.e.* the  
 412 fluid domain. The azimuthal velocity is not constrained to vanish at the inner and outer  
 413 boundaries, in order to account for the presence of thin unresolved boundary layers.

414 Azimuthal velocities are more than 10 times larger than the poloidal (*i.e.* meridional)  
 415 velocities. Nevertheless, the latter projects onto the ultrasound rays. We take the difference  
 416 of the profiles acquired for  $f$  and  $-f$  in order to eliminate this small contribution (the  
 417 meridional circulation does not change sign while the azimuthal velocity does).

418 FIG. 11 shows the isovalues of angular frequency  $f^*$  inverted for  $f = \pm 3$  Hz, with  
 419  $l_{max} = 3$  and  $k_{max} = 7$ . A crescent of super-rotation is present near the inner sphere.  
 420 There, isorotation contours roughly follow magnetic field lines, in agreement with Ferraro's  
 421 theorem, as anticipated above. At larger cylindrical distance from the inner sphere, the  
 422 flow becomes geostrophic: the contour lines are vertical. We note that angular velocities  
 423 just above the north pole of the inner sphere do not comply with Ferraro's law. Instead,  
 424 velocities decrease to quite low values inside the cylinder tangent to the inner sphere. Such  
 425 violations have been shown to occur when the electric conductivity of boundaries is high [51]  
 426 [50]. We speculate that we might be in this situation inside the tangent cylinder because the  
 427 opening of the sphere at the top and bottom (see FIG. 3) replaces the poorly conducting  
 428 stainless steel wall by sodium.

429 FIG. 11 compares the synthetic angular velocity profiles to the observed Doppler velocity  
 430 profiles along the various rays. Note that super-rotation is clearly visible in the raw profiles.

431 The drop in velocity just above the inner sphere is constrained by profiles 4 (green) and 6  
 432 (cyan), but its vertical extent is not.

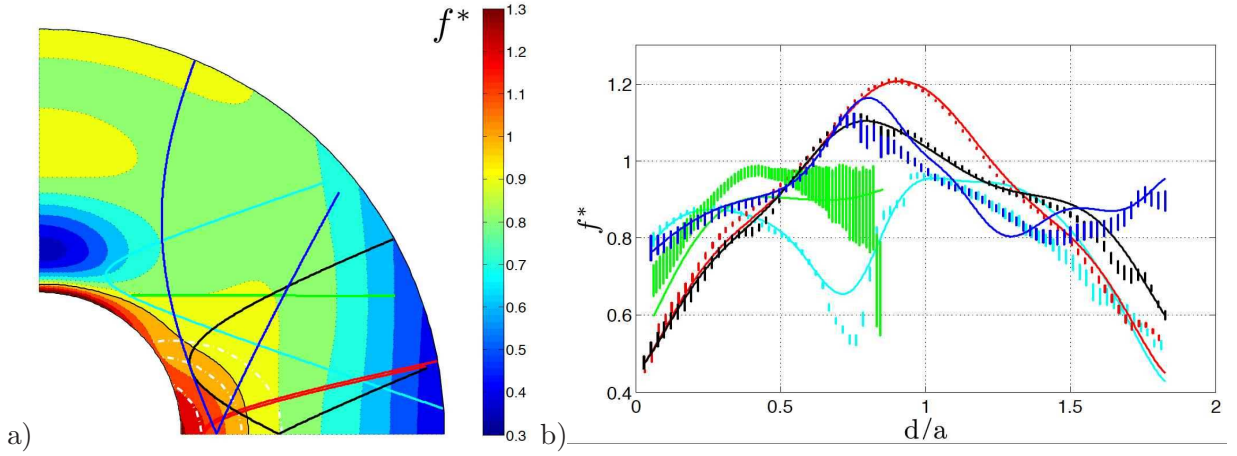


FIG. 11. a) Reconstructed isovalue map of fluid angular frequency  $f^*$  (the fluid angular frequency normalized by  $f$ ) at  $f = \pm 3$  Hz in a meridional plane, assuming axisymmetry and symmetry with respect to the equator. Super-rotation ( $f^* \gtrsim 1$ ) is clearly visible near the inner sphere, where the Ferraro law of isorotation applies. Contours become vertical further away, where geostrophy dominates. The fluid frequency is higher than 0.4 everywhere except in thin unresolved boundary layers. The color lines are the projection in the upper half  $(s, z)$  plane of the ultrasonic rays used in the inversion (see FIG. 3). b) Comparison between the measured ultrasonic Doppler  $f^*$  (shown by their error bars) and the synthetic profiles (solid lines) computed from the angular frequency map of Figure a) for  $f = \pm 3$  Hz. The  $x$ -axis gives the distance along the ray (in  $a$  units). The corresponding rays are plotted in Figure a) with the same color code.

### 433 C. $f_{fluid}$ deduced from differences in electric potential and from UDV

434 As in the previous study of *DTS* with rotating outer sphere [39], we observe that the  
 435 amplitudes of the differences in electric potential  $\Delta V$ 's vary linearly with  $\Delta V_{40}$ , the pro-  
 436 portionality factor increasing from the equator toward the poles due in particular to the  
 437 increase of  $B_r$  in formula (1). We show however in the present study that measuring the  
 438 electric potential does not yield a reliable indicator of the angular velocity  $f^*$  using formula  
 439 (1). In FIG. 12, we compare the normalized fluid angular velocity  $f^*$  retrieved from the  
 440  $\Delta V$ 's, for four different latitudes, to  $f^*$  obtained directly by UDV at the nearest measured

441 point, around  $d/a = 0.1$ . The frequencies  $f^*$  obtained from  $\Delta V$  and from UDV in FIG. 12,  
 442 would be similar if both measurement techniques were only sensitive to  $u_\varphi$  in the interior  
 443 below the outer viscous boundary layer. The strong discrepancy between these two sets of  
 444 frequencies reveals instead that the outer boundary layer in *DTS* cannot simply be reduced  
 445 to a Hartmann layer, outside of which the meridional currents  $j_\theta$  can be neglected. We  
 446 further discuss this point in the numerical part VI.

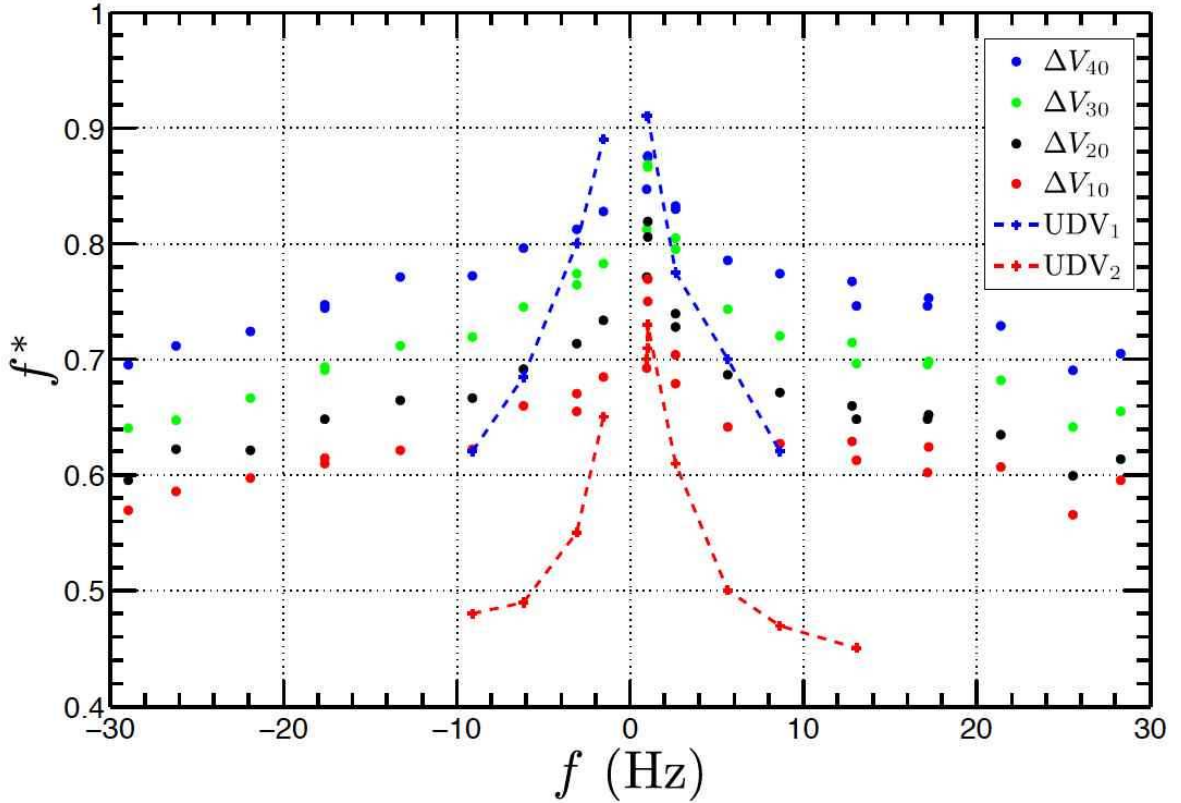


FIG. 12.  $f^*$  deduced from the measurements of  $\Delta V$  shown in a), using formula (1). Dashed blue line :  $f^*$  value obtained with UDV measurements on the trajectory number 1 at the distance  $d/a = 0.1$ . Dashed red line :  $f^*$  value obtained with UDV measurements on the trajectory number 2 for  $d/a = 0.1$ .

447 **V. MERIDIONAL CIRCULATION**

448 The meridional circulation is constrained from Doppler velocity profiles of the radial ve-  
 449 locity (shot along the radial direction), from profiles shot in a meridional plane, and from the  
 450 projection of the meridional velocity on "azimuthal" shots. The latter is obtained by taking  
 451 the sum of the profiles acquired for  $f$  and  $-f$ , in order to eliminate the azimuthal contribu-  
 452 tion. The same is done for the radial and meridional profiles to remove any contamination  
 453 from azimuthal velocities.

454 The poloidal velocity scalar  $u_P$  of equation (8) is expanded in associated Legendre func-  
 455 tions with even degree and order 1, *i.e.*

$$u_P(r, \theta) = \sum_{l=0}^{l_{max}} u_P^l(r) P_{2l}^1(\cos \theta). \quad (10)$$

456 The radial  $u_r$  and orthoradial  $u_\theta$  components of velocity are then obtained as:

$$u_r(r, \theta) = \sum_{l=0}^{l_{max}} \frac{u_P^l(r)}{r} \frac{1}{\sin \theta} \frac{d}{d\theta} (\sin \theta P_{2l}^1(\cos \theta)). \quad (11)$$

457

$$u_\theta(r, \theta) = - \sum_{l=0}^{l_{max}} \left( \frac{u_P^l(r)}{r} + \frac{du_P^l(r)}{dr} \right) P_{2l}^1(\cos \theta). \quad (12)$$

458 The functions  $u_P^l(r)$  are decomposed into a sum of  $\sin(k\pi(r - b/a)/(1 - b/a))$  from  $k = 0$   
 459 to  $k_{max}$ . The radial velocity is thus constrained to vanish at the inner and outer (rigid)  
 460 boundaries, but the orthoradial velocity is not, in order to account for the presence of thin  
 461 unresolved boundary layers. FIG. 13 shows the streamlines of the meridional circulation  
 462 inverted for  $f = \pm 3$  Hz, with  $l_{max} = 4$  and  $k_{max} = 8$ . The fluid is centrifuged from the  
 463 inner sphere in the equatorial plane and moves north in a narrow sheet beneath the outer  
 464 boundary. It loops back to the inner sphere in a more diffuse manner. Meridional velocities  
 465 are more than ten times weaker than azimuthal velocities.

466 FIG. 14 compares the synthetic radial and meridional profiles to the observed Doppler  
 467 velocity profiles along the various rays. Velocities are normalized by  $2\pi fa$ .

468 Over a decade (from  $f = 1.5$  Hz to  $= 15$  Hz), radial velocities are consistently centrifugal  
 469 at  $10^\circ$  latitude and centripetal at  $40^\circ$ , and are roughly proportional to  $f$ . The radial profiles  
 470 at  $20^\circ$  are more complex and evolve with  $f$ , indicating a non-monotonic evolution of the  
 471 meridional circulation, also evidenced by the records of the  $r$  and  $\theta$  components of the  
 472 induced magnetic field inside the fluid (see FIG. 6).

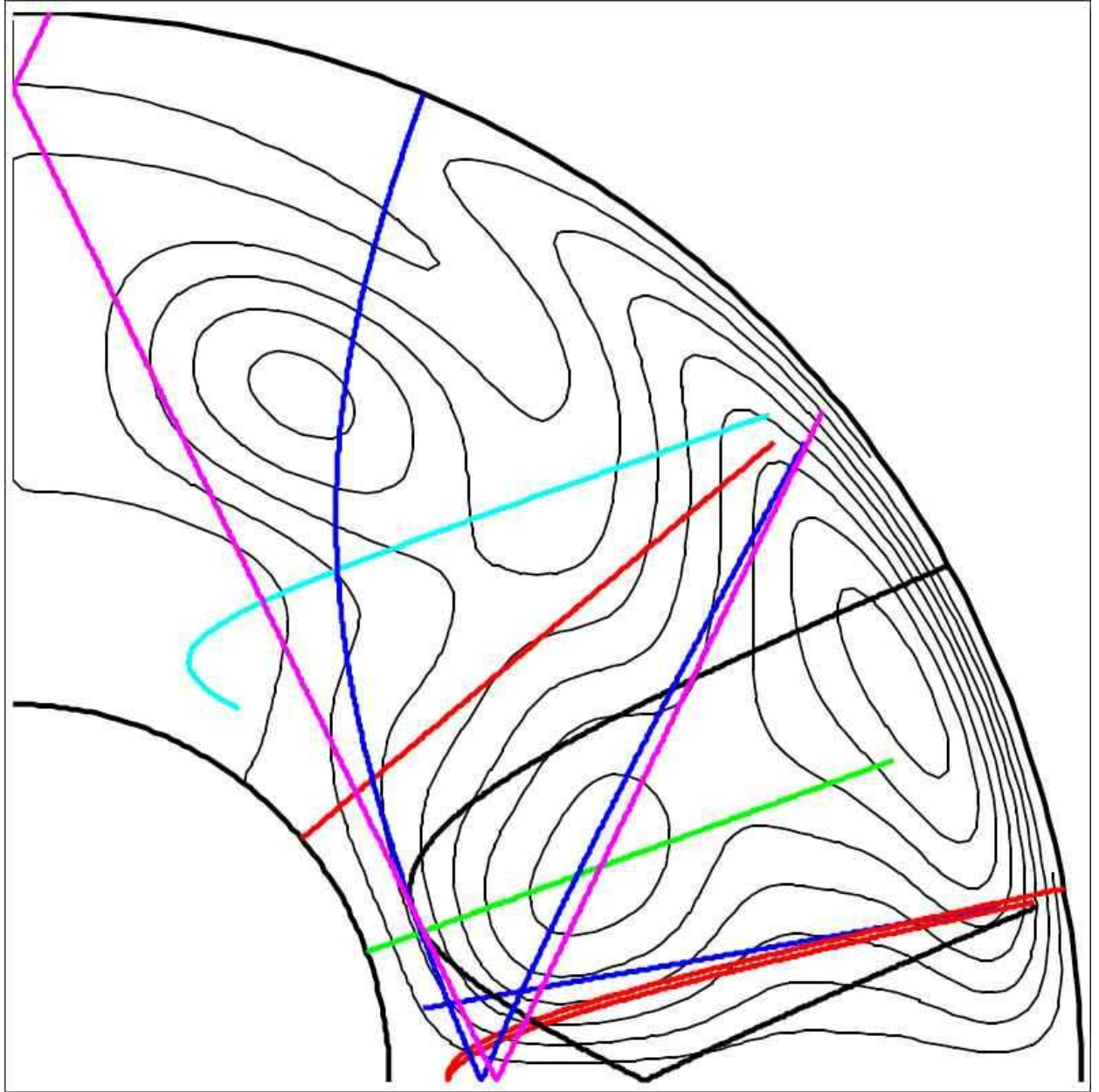


FIG. 13. Reconstructed stream lines of the meridional circulation at  $f = \pm 3$  Hz in a meridional plane, assuming axisymmetry and symmetry with respect to the equator. The interval between lines is  $1.6 \times 10^{-3}$ . The fluid is centrifuged away from the inner sphere in the equatorial region and moves up to the pole along the outer boundary. The color lines are the projection in the upper half  $(s, z)$  plane of the ultrasonic rays used in the inversion.

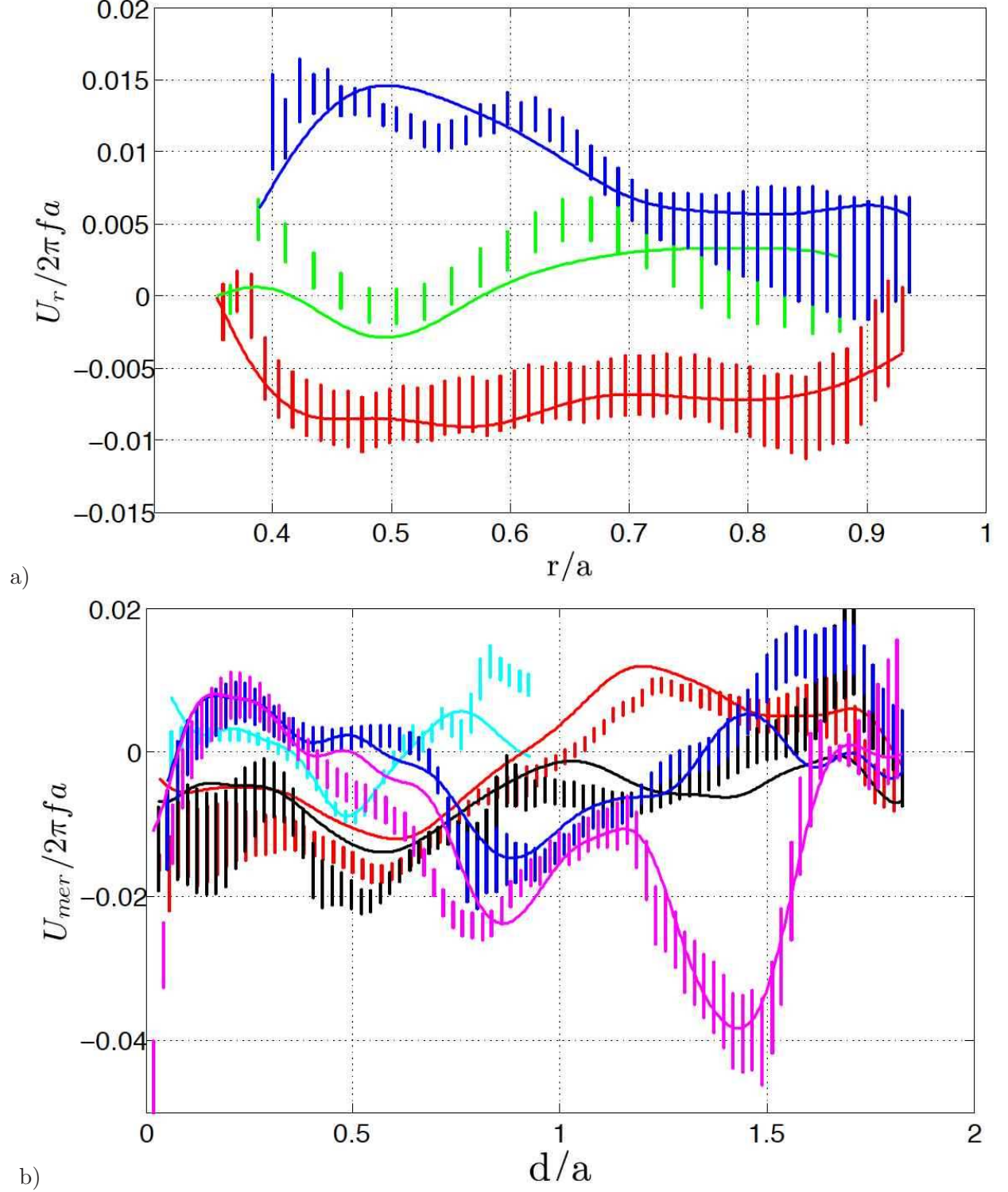


FIG. 14. Comparison between the measured ultrasonic Doppler velocity profiles (shown by their error bars) and the synthetic profiles (solid lines) computed from the meridional circulation map of FIG. 13 for  $f = \pm 3$  Hz. Radial profiles a), meridional and "azimuthal" profiles b). The contribution from the azimuthal flow has been removed by taking the sum of profiles acquired for  $f$  and  $-f$ . The  $x$ -axis gives the distance along the ray (in  $a$  units) and the  $y$ -axis is the velocity measured along the ray, adimensionalized by  $2\pi fa$ . The corresponding rays are plotted in FIG. 13 with the same color code.



## 473 VI. COMPARISON WITH NUMERICAL SIMULATIONS

474 Two previous numerical studies are particularly relevant to our work. Hollerbach et al.  
475 studied exactly the *DTS* configuration but for values of  $\Lambda$  much larger than its value in the  
476 experiment [29]. They focus their study on the modification of the linear solution by inertial  
477 effects, stressing that the magnetic field line tangent to the outer sphere at the equator loses  
478 its significance in the non linear regime. As a result of the relatively large value of  $\Lambda$ , the  
479 inertial effects remain too weak -when the outer sphere is at rest- to make a geostrophic  
480 region arise at large distances from the axis. The solutions of Garaud [52] (see the figures  
481 7 and 11) for a slightly different problem do show the transition between a Ferraro and a  
482 geostrophic regions. In her model, which pertains to the formation of the solar tachocline,  
483 a dipolar magnetic field permeates a thick spherical shell as in *DTS*, the rotation of the  
484 outer boundary is imposed and the rotation of the inner boundary is a free parameter: a  
485 condition of zero torque is imposed on that boundary. Numerical models [29, 39] of the  
486 *DTS* experiment when the outer sphere is rotating also clearly show a Ferraro region near  
487 the inner sphere where the magnetic field is strong and a geostrophic region in the vicinity  
488 of the equator of the outer sphere. We argue below that all these results obtained for a  
489 rotating outer sphere provide us with a useful guide to interpret the numerical solutions  
490 when the outer sphere is at rest.

### 491 A. The numerical model

492 The model consists of four nested spherical layers (see FIG. 15). The fluid layer is enclosed  
493 between a weakly conducting outer container and a central solid sphere comprised of an inner  
494 insulating core and of a strongly conducting outer envelope.

495 The velocity field is decomposed as stated in the definitions (8) and (9). The variables  
496  $u_\varphi^l(r)$  and  $u_p^l(r)$  are then discretized in radius. Analogous decompositions of variables de-  
497 noted  $b_\varphi^l(r)$  and  $b_p^l(r)$  are employed to represent the induced magnetic field. The truncation  
498 level  $lmax$  (see (9)) is 120 and at least 450 unevenly spaced points are used in the radial  
499 direction.

500 The equations (4) and (5), modified to include all the non linearities and the time deriva-  
501 tives of  $\mathbf{u}$  and  $\mathbf{b}$ , are transformed into equations for  $u_\varphi^l$ ,  $u_p^l$ ,  $b_\varphi^l$  and  $b_p^l$ .

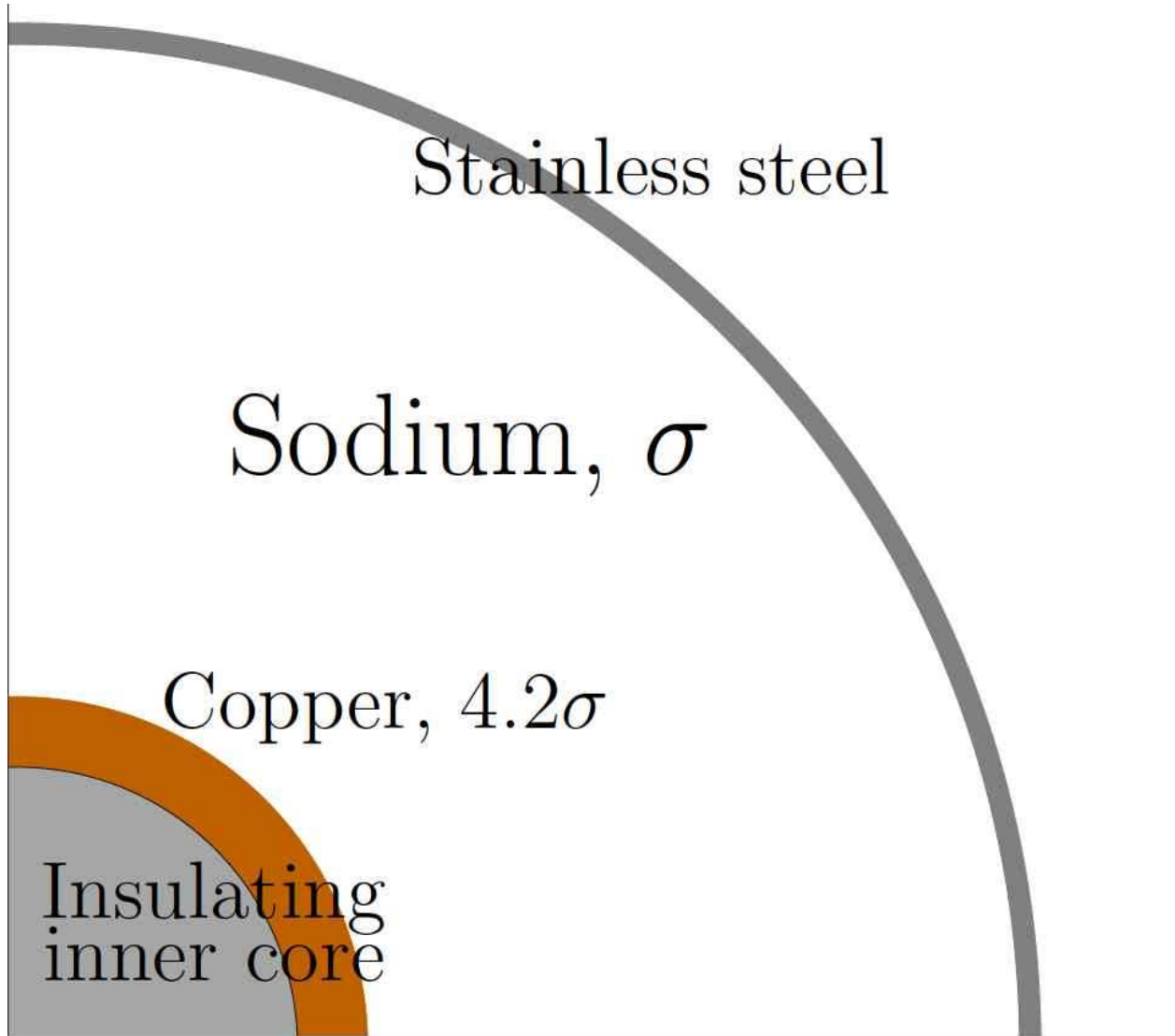


FIG. 15. Geometry of the numerical model. The relative conductance of the solid outer shell is  $\sigma_b \delta / \sigma a = 1/336$ , with  $\sigma_b$  and  $\delta$  respectively the conductivity and the thickness of the outer sphere. It reproduces the experimental value with  $\sigma_b$  chosen as the conductivity of stainless steel at  $140^\circ\text{C}$ . The conductivity ratio between the layers 2 and 3 reproduces the ratio (4.2) between the conductivity of copper and sodium.

502 The dimensionless numbers  $\text{Re}$  and  $\Lambda$  are chosen so that steady solutions exist and are  
 503 stable, with  $\text{Pm} \ll 1$  ( $\text{Pm}$  enters the definition of the unit induced field). Solutions are  
 504 obtained after time-stepping the equations until a stationary state is reached. They have  
 505 been successfully compared to solutions obtained with another numerical code PARODY,

506 which is not restricted to axisymmetric variables [53] [26].

507 It is not possible to simulate the Reynolds number of the experiment, which is about  $10^6$ .  
508 For the experimental range of  $\Lambda$ , steady solutions are obtained with  $\text{Re} \sim 10^3$ .

## 509 B. Steady axisymmetric solutions

510 FIG. 16 displays a typical solution for the angular and meridional velocities that illustrates  
511 well the experimental results. The fluid rotates faster than the magnetized inner body in its  
512 vicinity. There, the angular velocity is constant along magnetic field lines of force. Further  
513 away of the inner core, the zonal shear becomes almost geostrophic. In addition to these  
514 features that we have retrieved from the experimental results, the numerical solution displays  
515 recirculation in the outer boundary layer at high latitude. There, the interior flow largely  
516 consists in rigid rotation and the boundary layer has the characteristics of a Bödewadt layer  
517 with a region of enhanced angular rotation.

518 For large enough  $\text{Re}$  (*e.g.*  $(a/b)^2\text{Re} = 10^4$  with  $(b/a)^2\text{Ha} = 20$ ), circular waves are present  
519 in the Bödewadt layer, above  $60^\circ$  of latitude. They propagate towards the axis. Similar waves  
520 had been reported before in simulations of the flow between a rotating and a stationary disk  
521 in the absence of a magnetic field [54]. There, they eventually die out. Thus, the persistence  
522 of propagation of circular waves in the boundary layer attached to the sphere at rest may  
523 be attributed to the presence of a magnetic field. On the other hand, these waves arise for  
524 larger  $\text{Re}$  as  $\text{Ha}$  is augmented. Their emergence delimits the domain of steady solutions.

525 We have checked that the thickness of the outer boundary layer in the numerical solution  
526 scales as  $\Omega^{-1/2}$ . Note that it corresponds to 3 mm for  $\Omega = 1.5 \text{ s}^{-1}$  and the viscosity of  
527 liquid sodium. The fluid rotation is driven by the electromagnetic torque acting at the inner  
528 boundary against the viscous torque at the outer boundary. We have found that both the  
529 viscous torque on the inner surface and the electromagnetic torque on the outer surface are  
530 negligible. Comparing different simulations, we have also checked that the main viscous  
531 torque scales as  $\sim \Omega^{3/2}$ , as expected from the thickness of the Bödewadt layer. Thus, the  
532 power required to drive the fluid rotation scales as  $\Omega^{5/2}$ , as does the experimentally measured  
533 power (see section IID).

534 The angular rotation just below the outer viscous layer scaled by the inner core angular  
535 rotation decreases with  $\text{Re}$  in agreement with the experimental results. On the other hand,

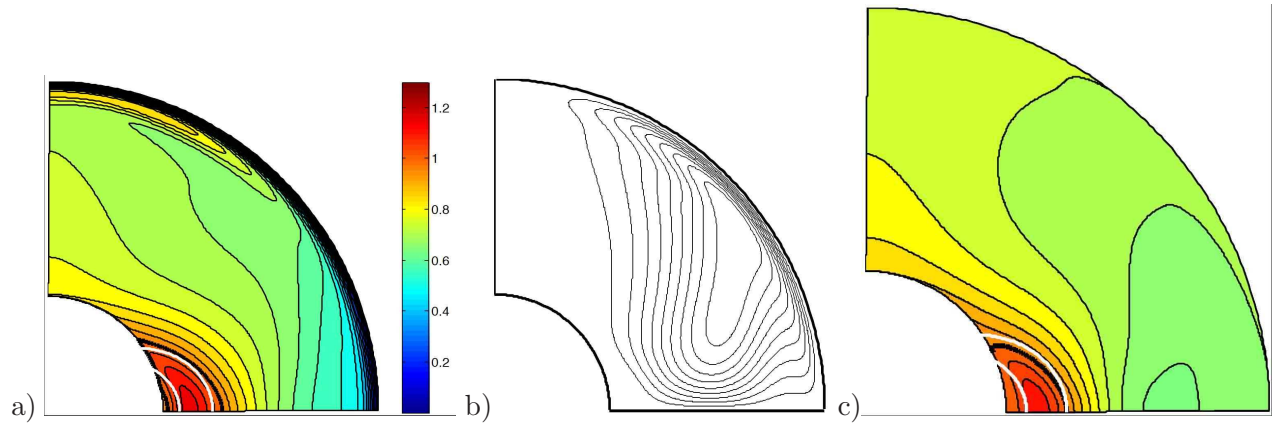


FIG. 16. a) Angular and b) meridional velocity in a meridional plane for  $Re = 9.5 \cdot 10^2$ ,  $Ha = 163$ , and  $Pm = 10^{-3}$ . c) angular velocity estimated from  $V$ , using (1). Two dipolar field lines (thick and white) are superimposed in the angular velocity maps, and the thick contour line is where the angular velocity is unity.

536 the angular rotation that would be inferred from the electric potential differences calculated  
 537 at the outer surface using expression (1) increases with  $\text{Re}$ . FIG. 16c displays the angular  
 538 velocity as estimated from the electric potential, according to equation (1). It can be com-  
 539 pared to FIG. 16a. The actual shear is well retrieved where the magnetic force predominates,  
 540 in the region where Ferraro's law of isorotation holds. There, the electric current density  $\mathbf{j}$  is  
 541 limited by the strength of the magnetic force, which needs to be balanced by another force.  
 542 That restriction makes it possible to neglect  $\mathbf{j}$  in Ohm's law. Then, predictions made from  
 543 (1) are correct. On the other hand, the actual shear is not well recovered in the geostrophic  
 544 region where the electric current density is not limited by the strength of the magnetic field.  
 545 There, the frozen-flux relation (1) can be violated. We thus explain why the electric poten-  
 546 tial measurements at the surface of the *DTS* experiment do not yield a good prediction of  
 547 the angular velocity immediately below the outer viscous boundary layer.

548 Our first discussion [30] of the electric potential measurements was based on a numerical  
 549 model calculated for the experimental values of  $\text{Ha}$  and thus for too large values of  $\Lambda$ . As a  
 550 result, the magnetic force, in the numerical model, was dominant in the entire fluid layer and  
 551 the frozen-flux relationship (1) was verified, at least away from the equator where  $B_r = 0$ .  
 552 However, equation (1), becomes less and less valid as  $\text{Re}$  is increased and  $\Lambda$  decreased, in  
 553 agreement with the divergence that has been experimentally observed (see the FIG. 12)  
 554 between the angular velocity calculated from (1) and the actual velocity.

555 Incidentally, cranking up the rotation of the magnetized inner sphere stabilizes the fluid  
 556 circulation, at least within a certain parameter range. We have calculated the time-averaged  
 557 solution (not shown) for the same parameters as the steady solution illustrated by FIG. 16,  
 558 but for a lower  $\text{Re}$ . Both the flow and the induced magnetic field are periodic for this set of  
 559 parameters. A second meridional roll, which is centripetal in the equatorial plane, turns up  
 560 in the outer region. There, it creates a disk-shaped region where the rotation is slow and  
 561 the solution is strikingly different from the almost geostrophic solution (FIG. 16) obtained  
 562 for a slightly larger value of  $\text{Re}$ .

### 563 C. Comparison between numerical simulations and experimental results

564 We find that reproducing the Elsasser number  $\Lambda$ , rather than a combination of  $\Lambda$  and  $\text{Re}$   
 565 such as the Hartmann number  $\text{Ha} = (\text{Re}\Lambda)^{1/2}$ , is the key factor to recover the experimental

566 results. The parameters for the solution displayed in FIG. 16 correspond to  $\Lambda = 28$ , which  
 567 is the appropriate value for experiments with  $\Omega = 1.5 \text{ s}^{-1}$ . With  $\text{Pm} = 10^{-3}$ , the value of  
 568 the magnetic Reynolds number is about right. It remains too small for the poloidal field to  
 569 be much different from the imposed dipole field (again for the parameters of FIG. 16).

570 FIG. 17 shows that numerical solutions are able to satisfactorily reproduce the ultrasonic  
 571 measurements of angular velocity, obtained for the same values of  $\Lambda$ , as expected from the  
 572 similitude of the angular velocity maps 16 and 11. The simulated velocities have weaker  
 573 amplitude than the measured ones in much of the fluid though. We have checked that  
 574 increasing  $\text{Re}$ , whilst keeping  $\Lambda$  constant, favours enhanced corotation between the fluid  
 575 and the inner core. As our calculations are for much smaller  $\text{Re}$  than the values realized in  
 576 the experiment, that result may explain the remaining discrepancy between measured and  
 577 simulated velocities.

## 578 VII. DISCUSSION AND CONCLUSION

579 In the presence of an imposed magnetic field, which favors solid body rotation, the inertial  
 580 forces largely reduce to a Coriolis force, even for large Reynolds numbers. Experimental  
 581 results can thus be interpreted using a single dimensionless number, the Elsasser number.  
 582 In that respect, experimental results obtained with global rotation [39] provide a better  
 583 guide to interpreting the present results than the linear situation studied by Dormy et al.  
 584 [28, 31]. We estimate that, in *DTS*, the rotation frequency  $f$  should be less than 0.1 Hz for  
 585 the latter to be approached.

586 Experiments have been conducted with the inner sphere rotating in the range -30 Hz  
 587  $\leq f \leq 30$  Hz. We have been able to map extensively the shear in the fluid cavity from  
 588 Ultrasonic Doppler velocimetry for  $|f| \leq 10$  Hz. Our observations provide a very clear  
 589 experimental illustration of Ferraro's law of isorotation, demonstrating the predominance  
 590 of magnetic forces near the inner sphere. They also exhibit a strong super-rotation: in the  
 591 region where magnetic forces dominate, the fluid angular velocity gets 30% larger than that  
 592 of the inner sphere. This contrasts with the results obtained by Dormy et al [28] when global  
 593 rotation is present, which indicate that the phenomenon of super-rotation is hindered by the  
 594 Coriolis force. The experimental results obtained in our previous study with global rotation  
 595 [39] could not address this issue and we plan to run additional experiments for that purpose.

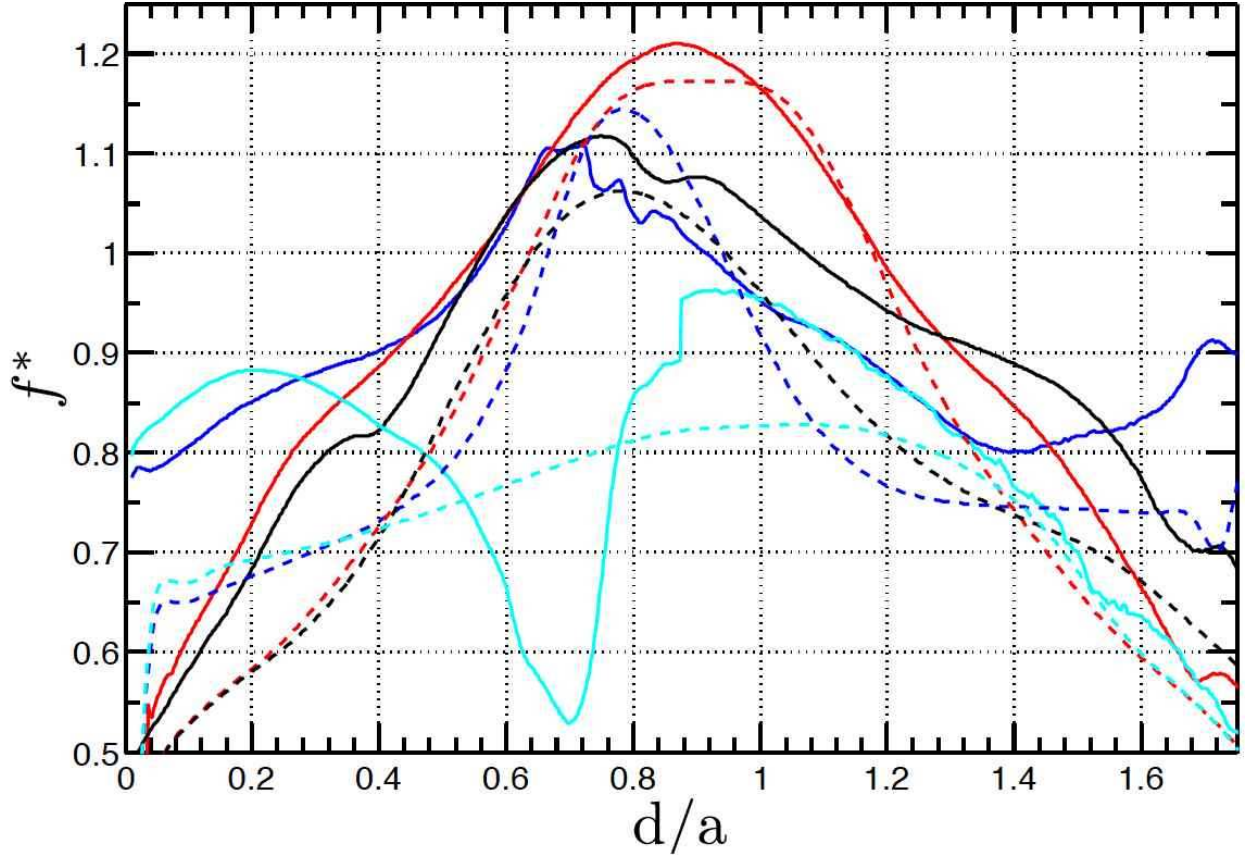


FIG. 17. Angular velocity along the ultrasonic rays as a function of the distance from the probe: measured (solid lines, 3 Hz,  $\Lambda = 16$ ) and retrieved from a time-averaged numerical solution (dashed lines,  $\text{Re} = 1.5 \cdot 10^3$ ,  $\text{Ha} = 163$ ,  $\text{Pm} = 10^{-3}$ ,  $\Lambda = 18$ ). The error bars of the experimental data are shown in FIG. 11.

596 The experiments also display a clear violation to Ferraro's law: quite low angular velocities  
597 are observed just above the inner sphere, where the magnetic field is strongest (see FIG. 11).  
598 We suspect that this is due to the presence of sodium at rest at the top and bottom of the  
599 cylinder tangent to the inner sphere. Indeed, such violations have been shown to occur when  
600 the electric conductivity of boundaries is high [51] [50].

601 We could follow the evolution of induced magnetic field, electric potentials and power  
602 across the full range of forcing. In a first approximation, all observables associated with the  
603 azimuthal flow (which dominates) can be described by a universal solution, both velocities  
604 and induced magnetic field scaling with  $f$ . In a second approximation, the increase of the  
605 dimensional fluid velocity with  $f$  thins the viscous boundary layer at the outer sphere and

606 increases friction accordingly, thus reducing the adimensional velocity of the fluid inside  
 607 the sphere. At the same time, the effective Coriolis force that results from the non-linear  
 608  $(\mathbf{u} \cdot \nabla)\mathbf{u}$  term increases with respect to the (linear) Lorentz force: the geostrophic region  
 609 extends further towards the inner sphere. This explains that the fluid velocity increases with  
 610  $f$  less rapidly than  $f$  (FIG. 5) at large  $f$  whilst the torque instead increases more rapidly  
 611 than  $f$  (FIG. 4) (the electric potentials follow an intermediate trend). The outer friction  
 612 torque is balanced by the magnetic torque at the inner boundary. This is consistent with  
 613 an increase of the induced magnetic field, near the solid inner body, that is steeper than  $f$   
 614 (see FIG. 6). On the other hand, the description of Nataf and Gagnière [55] pertains to the  
 615 region where the shear is geostrophic. There, the increased torque at the outer boundary is  
 616 balanced by the magnetic torque on the geostrophic cylinders in the interior, which results  
 617 from the shearing of the imposed dipolar field. The direct measurement of the velocity (up to  
 618 10 Hz, see FIG. 9) shows that the adimensionalized shear does not change significantly with  
 619  $f$  even though the velocity itself decreases. In addition, the induced azimuthal magnetic  
 620 field that we measure inside the sphere (FIG. 6), for the whole range of  $f$ , increases more  
 621 rapidly than  $f$ . At large  $f$ , we observe that  $b_\varphi$  gets larger than the imposed dipolar field in  
 622 much of the fluid layer. Eventually, this induced field is large enough to modify the overall  
 623 magnetic field, and the resulting flow.

624 This last regime, only achieved because the magnetic Reynolds number is large enough,  
 625 is probably the most interesting one. Unfortunately, we cannot directly measure the flow  
 626 velocities with the ultrasound technique at these very large  $f$ . Less direct techniques are  
 627 now required to investigate the zonal shear for  $f > 10$  Hz. Inertial waves modified in the  
 628 presence of the dipolar and the induced magnetic fields have been inferred from records of  
 629 the electric potential along parallels at the surface [41] and of the magnetic field along a  
 630 meridian. Both their period and their wavenumber vary with the geometry of the differential  
 631 rotation in the cavity. Hopefully, it will be possible to invert the zonal shear from the records  
 632 of magneto-inertial waves.

633 Guided by the numerical model, we find that electric field measurements are difficult to  
 634 interpret, particularly in the equatorial region where the radial magnetic field  $B_r$  vanishes.  
 635 The frozen-flux approximation (1) holds when there is a mechanism that keeps under control  
 636 the strength of the electrical currents [56]. This is the reason why the magnetic Reynolds  
 637 number  $Rm$  is not relevant to discuss the validity of the frozen-flux approximation in our



638 quasi-steady experiment. That approximation has predictive power, instead, in regions  
639 where the magnetic force is dominating. In the *DTS* experiment, it corresponds to the  
640 inner region close to the magnet where  $\Lambda \geq 1$ .

641 In a geophysical context, a similar approach is routinely used [57] to invert the velocity  
642 field at the Earth's core surface from models of the time changes of the geomagnetic field,  
643 the so-called secular variation. Taking the example of a quasi steady state, this geophysical  
644 application has been criticized from a strictly kinematic standpoint [58]. We reckon in-  
645 stead that it is necessary to consider the balance of forces to decide whether the frozen-flux  
646 hypothesis holds, at least for a quasi steady state as illustrated by the *DTS* experiment.

647 Features of the experiment that only depend upon dimensionless numbers that do not  
648 involve diffusivities have been simulated numerically. An analogous explanation has been  
649 put forward to explain the intriguing successes of geodynamo simulations [5].

## 650 **ACKNOWLEDGMENTS**

651 The *DTS* project has been supported by Fonds National de la Science, Agence Nationale  
652 de la Recherche (Research program VS-QG, grant number BLAN06-2.155316), Institut Na-  
653 tional des Sciences de l'Univers, Centre National de la Recherche Scientifique, and Université  
654 Joseph-Fourier. We are thankful to Dominique Grand and his colleagues from *SERAS* who  
655 conducted the design study of the mechanical set-up. The magnetic coupler was computed  
656 by Christian Chillet.

657 **Appendix: Angular and meridional velocity along the ultrasonic oblique rays**

658 The seven oblique ultrasonic rays shot in *DTS* are sketched in FIG. 3. We define the  
 659 declination  $D$  as the angle between the beam and the meridional plane ( $D$  counted positively  
 660 eastwards), the inclination  $I$  as the angle between the projected beam in the meridional plane  
 661 and the radial direction ( $I$  counted positively upwards) and  $\lambda$  as the latitude of the ultrasonic  
 662 probe. Using those definitions, TABLE III give the characteristics of the beams.

TABLE III. Latitude  $\lambda$ , inclination  $I$ , and declination  $D$  (in degrees) at the origin of the shots (on the outer sphere) of the oblique ultrasonic beams in *DTS*.

Trajectory number and color	$\lambda$	$I$	$D$
1, blue	40	21.1	11.7
2, red	10	2.2	23.9
3, black	10	12.5	-20.6
4, green	-20	20	-13.5
5, yellow	-20	21.1	-11.7
6, cyan	-40	21.1	11.7
7, magenta	-40	-24	0

663 **1. Angular velocity**

664 Along these oblique beams, the projection  $u(d)$  ( $d$  is the distance from the probe) of the  
 665 velocity is a combination of the components  $u_r$ ,  $u_\theta$  and  $u_\varphi$  of the total velocity field. Velocity  
 666  $u(d)$  is counted positive in the shooting direction. We assume that the mean fluid flow is  
 667 axisymmetric, and also  $(u_r, u_\theta) \ll u_\varphi$ , the meridional velocities amplitude in *DTS* being less  
 668 than 10 % the amplitude of the azimuthal velocities. Using projections along the beam, we  
 669 retrieve the angular velocity  $\omega(d)$  along trajectories 1 to 6 using the following relationship

$$\omega(d) = -\frac{u(d)}{a \cos \lambda \sin D}. \quad (\text{A.1})$$

670 **2. Meridional velocity**

671 We have also exploited the observation that the meridional velocity does not change sign  
 672 when the rotation of the inner sphere is reversed - it remains centrifugal in the equatorial  
 673 plane - whereas the angular velocity does change sign. Thus, combining measurements  
 674 obtained with two opposite rotation rates of the inner core, we can separate azimuthal and  
 675 meridional velocities.

676 Assuming now that the mean meridional velocity is axisymmetric and using projections,  
 677 we can retrieve the radial velocity

$$u_r(d) = \frac{u(d)r(d)}{d - a \cos D \cos I}, \quad (\text{A.2})$$

678 and the orthoradial velocity

$$u_\theta(d) = \frac{u(d)r(d)s(d)}{a[a \cos D \cos \lambda \sin I - d \cos^2 D \cos(\lambda + I) \sin I + d \sin^2 D \sin \lambda]}, \quad (\text{A.3})$$

679 where  $r(d) = \sqrt{x^2 + y^2 + z^2}$  is the spherical radius and  $s(d) = \sqrt{x^2 + y^2}$  is the cylindrical  
 680 radius at the measurement point. They  $(x, y, z)$  coordinates of the measurement point are  
 681 given by:

$$x(d) = a \cos \lambda - d \cos D \cos(\lambda + I) \quad (\text{A.4})$$

$$y(d) = -d \sin D \quad (\text{A.5})$$

$$z(d) = a \sin \lambda - d \cos D \sin(\lambda + I) \quad (\text{A.6})$$

---

682 [1] W. M. Elsasser, *Phys. Rev.*, **69**, 106 (1946).  
 683 [2] W. M. Elsasser, *Phys. Rev.*, **70**, 202 (1946).  
 684 [3] J. Verhoogen, *Energetics of the Earth* (National Academy of Sciences, Washington, 1980).  
 685 [4] G. A. Glatzmaier and P. H. Roberts, *Nature*, **377**, 203 (1995).  
 686 [5] U. Christensen and J. Aubert, *Geophys. J. Int.*, **166**, 97 (2006).  
 687 [6] F. Takahashi, M. Matsushima, and Y. Honkura, *Phys. Earth Planet. Inter.*, **167**, 168 (2008).  
 688 [7] A. Sakuraba and P. Roberts, *Nature Geoscience* (2009).  
 689 [8] E. Dormy, J.-P. Valet, and V. Courtillot, *Geochem. Geophys. Geosyst.*, **1** (2000), doi:  
 690 10.1029/2000GC000062, 2000.

- 691 [9] J.-P. Poirier, *Introduction to the Physics of the Earth's Interior* (Cambridge University Press,  
692 Cambridge, UK, 2000).
- 693 [10] E. Dormy and A. M. Soward, *Mathematical aspects of natural dynamos* (CRC Press/Taylor  
694 Francis, 2007).
- 695 [11] A. Gailitis, O. Lielausis, E. Platacis, S. Dement'ev, A. Cifersons, G. Gerbeth, T. Gundrum,  
696 F. Stefani, M. Christen, and G. Will, *Phys. Rev. Lett.*, **86**, 3024 (2001).
- 697 [12] R. Stieglitz and U. Müller, *Phys. Fluids*, **13**, 561 (2001).
- 698 [13] Y. Ponomarenko, *J. Appl. Mech. Tech. Phys.*, **14**, 775 (1973).
- 699 [14] G. O. Roberts, *Phil. Trans. R. Soc. London, Ser. A*, **271**, 411 (1972).
- 700 [15] M. Berhanu, R. Monchaux, S. Fauve, N. Mordant, F. Pétrélis, A. Chiffaudel, F. Daviaud,  
701 B. Dubrulle, L. Marié, F. Ravelet, M. Bourgoin, P. Odier, J.-F. Pinton, and R. Volk, *Europhys.*  
702 *Lett.*, **77**, 59001 (2007).
- 703 [16] R. Monchaux, M. Berhanu, M. Bourgoin, M. Moulin, P. Odier, J.-F. Pinton, R. Volk, S. Fauve,  
704 N. Mordant, F. Pétrélis, A. Chiffaudel, F. Daviaud, B. Dubrulle, C. Gasquet, L. Marié, and  
705 F. Ravelet, *Phys. Rev. Lett.*, **98**, 044502 (2007).
- 706 [17] D. R. Sisan, N. Mujica, W. A. Tillotson, Y.-M. Huang, W. Dorland, A. B. Hassam, T. M.  
707 Antonsen, and D. P. Lathrop, *Phys. Rev. Lett.*, **93**, 114502 (2004).
- 708 [18] M. D. Nornberg, E. J. Spence, R. D. Kendrick, C. M. Jacobson, and C. B. Forest, *Phys. Rev.*  
709 *Lett.*, **97**, 044503 (2006).
- 710 [19] F. Petrelis, N. Mordant, and S. Fauve, *Geophys. Astrophys. Fluid Dyn.*, **101**, 289 (2007).
- 711 [20] J. Taylor, *Proc. R. Soc. Lond. A*, **274**, 274 (1963).
- 712 [21] P. Cardin, D. Brito, D. Jault, H.-C. Nataf, and J.-P. Masson, *Magnetohydrodynamics*, **38**,  
713 177 (2002).
- 714 [22] D. Jault, *Phys. Earth Planet. Inter.*, **166**, 67 (2008).
- 715 [23] F. H. Busse, *J. Fluid Mech.*, **44**, 441 (1970).
- 716 [24] X. Song and P. Richards, *Nature*, **382**, 221 (1996).
- 717 [25] N. Schaeffer and P. Cardin, *Earth Planet. Sci. Lett.*, **245**, 595 (2006).
- 718 [26] C. Guervilly and P. Cardin, *Geophys. Astrophys. Fluid Dyn.*, **104**, 221 (2010).
- 719 [27] R. Hollerbach, *Proc. R. Soc. Lond. A*, **444**, 333 (1994).
- 720 [28] E. Dormy, P. Cardin, and D. Jault, *Earth Planet. Sci. Lett.*, **160**, 15 (1998).
- 721 [29] R. Hollerbach, E. Canet, and A. Fournier, *Eur. J. Mech. B*, **26**, 729 (2007).

- 722 [30] H.-C. Nataf, T. Alboussière, D. Brito, P. Cardin, N. Gagnière, D. Jault, J.-P. Masson, and  
723 D. Schmitt, *Geophys. Astrophys. Fluid Dyn.*, **100**, 281 (2006).
- 724 [31] E. Dormy, D. Jault, and A. M. Soward, *J. Fluid Mech.*, **452**, 263 (2002).
- 725 [32] V. Ferraro, *Mon. Not. Roy. Astron. Soc.*, **97**, 458 (1937).
- 726 [33] H. Spruit, *Astron. Astrophys.*, **349**, 189 (1999).
- 727 [34] C. Charbonnel and S. Talon, *Science*, **309**, 2189 (2005).
- 728 [35] K. MacGregor and P. Charbonneau, *Astrophys. J.*, **519**, 911 (1999).
- 729 [36] L. Mestel and N. Weiss, *Mon. Not. Roy. Astron. Soc.*, **226**, 123 (1987).
- 730 [37] D. Gough, in *Magnetic Coupling between the Interior and Atmosphere of the Sun*, edited by  
731 S. Hasan and R. Rutten (Springer, 2010) pp. 68–85.
- 732 [38] J. Aubert, *J. Fluid Mech.*, **542**, 53 (2005).
- 733 [39] H.-C. Nataf, T. Alboussière, D. Brito, P. Cardin, N. Gagnière, D. Jault, and D. Schmitt, *Phys.*  
734 *Earth Planet. Inter.*, **170**, 60 (2008).
- 735 [40] N. Kleeorin, I. Rogachevskii, A. Ruzmaikin, A. M. Soward, and S. Starchenko, *J. Fluid Mech.*,  
736 **344**, 213 (1997).
- 737 [41] D. Schmitt, T. Alboussière, D. Brito, P. Cardin, N. Gagnière, D. Jault, and H.-C. Nataf, *J.*  
738 *Fluid Mech.*, **604**, 175 (2008).
- 739 [42] Y. Takeda, *Nucl. Technol.*, **79**, 120 (1987).
- 740 [43] D. Brito, H.-C. Nataf, P. Cardin, J. Aubert, and J.-P. Masson, *Exp. Fluids*, **31**, 653 (2001).
- 741 [44] J. Noir, D. Brito, K. Aldridge, and P. Cardin, *Geophys. Res. Lett.*, **28**, 3785 (2001).
- 742 [45] J. Aubert, D. Brito, H.-C. Nataf, P. Cardin, and J.-P. Masson, *Phys. Earth Planet. Inter.*,  
743 **128**, 51 (2001).
- 744 [46] N. Gillet, D. Brito, D. Jault, and H.-C. Nataf, *J. Fluid Mech.*, **580**, 83 (2007).
- 745 [47] S. Eckert and G. Gerbeth, *Exp. Fluids*, **32**, 542 (2002).
- 746 [48] S. Fauve and D. Lathrop, *Fluid Dynamics and Dynamos in Astrophysics and Geophysics*,  
747 edited by A. M. Soward, C. Jones, D. Hughes, and N. Weiss (CRC Press, 2005) pp. 393–426.
- 748 [49] K. Mizerski and K. Bajer, *Phys. Earth Planet. Inter.*, **160**, 245 (2007).
- 749 [50] A. Soward and E. Dormy, *J. Fluid Mech.*, **645**, 145 (2010).
- 750 [51] J. Allen, P. Auer, and V. Endean, *Plasma physics*, **18**, 143 (1976).
- 751 [52] P. Garaud, *Mon. Not. Roy. Astron. Soc.*, **329**, 1 (2002).
- 752 [53] J. Aubert, J. Aurnou, and J. Wicht, *Geophys. J. Int.*, **172**, 945 (2008).

- 753 [54] J. Lopez, F. Marques, A. Rubio, and M. Avila, *Phys. Fluids*, **21**, 114107 (2009).
- 754 [55] H.-C. Nataf and N. Gagnière, *C.R. Physique*, **9**, 702 (2008).
- 755 [56] D. Jackson, *Classical Electrodynamics* (John Wiley, New York, 1975).
- 756 [57] R. Holme, *Treatise on Geophysics, Vol. 8 Core Dynamics*, edited by P. Olson and G. Schubert  
757 (Elsevier, 2007) Chap. 8.04, pp. 107–129.
- 758 [58] J. J. Love, *Geophys. J. Int.*, **138**, 353 (1999).